UC San Diego
UC San Diego Previously Published Works

Title
Corticostriatal Flow of Action Selection Bias

Permalink
https://escholarship.org/uc/item/1qx1n02b

Journal
Neuron, 104(6)

ISSN
0896-6273

Authors
Hwang, Eun Jung
Link, Trevor D
Hu, Yvonne Yuling
et al.

Publication Date
2019-12-01

DOI
10.1016/j.neuron.2019.09.028

Peer reviewed

Corticostriatal flow of action selection bias

Eun Jung Hwang[1,*], **Trevor D. Link**[1], **Yvonne Yuling Hu**[1,2], **Shan Lu**[1,3], **Eric Hou-Jen Wang**[4], **Varoth Lilascharoen**[1], **Sage Aronson**[1,5], **Keelin O'Neil**[1,6], **Byung Kook Lim**[1], **Takaki Komiyama**[1,7,*]

[1]Neurobiology Section, Center for Neural Circuits and Behavior, and Department of Neurosciences, University of California San Diego, La Jolla, CA 92093, USA

[2]Department of Photonics, National Cheng Kung University, Tainan, Taiwan

[3]Department of Biological Sciences, Columbia University, New York, NY 10027, USA

[4]Biomedical Sciences Graduate Program, University of California San Diego, La Jolla, CA, 92039, USA

[5]Neurophotometrics, San Diego, CA 92121, USA

[6]NYU Neuroscience Institute, New York University School of Medicine, New York, NY 10016, USA

[7]Lead contact

Summary

The posterior parietal cortex (PPC) performs many functions, including decision-making and movement control. It remains unknown which input and output pathways of PPC support different functions. We addressed this issue in mice, focusing on PPC neurons projecting to the dorsal striatum (PPC-STR) and the posterior secondary motor cortex (PPC-pM2). Projection-specific, retrograde labeling showed that PPC-STR and PPC-pM2 represent largely distinct subpopulations, with PPC-STR receiving stronger inputs from association areas and PPC-pM2 receiving stronger sensorimotor inputs. Two-photon calcium imaging during decision-making revealed that the PPC-STR population encodes history-dependent choice bias more strongly than PPC-pM2 or general PPC populations. Furthermore, optogenetic inactivation of PPC-STR neurons or their terminals in STR decreased history-dependent bias, while inactivation of PPC-pM2 neurons altered movement kinematics. Therefore, PPC biases action selection through its STR projection, while controlling movements through PPC-pM2 neurons. PPC may support multiple functions through parallel subpopulations, each with distinct input-output connectivity.

*Correspondence: tkomiyama@ucsd.edu (TK), eunjunghwang.phd@gmail.com (EJH).

eTOC

The posterior parietal cortex (PPC) is important for both action selection and sensorimotor control. Using projection-specific anatomical tracing, activity recording, and perturbation, Hwang et al. identified two parallel subsystems in PPC, each involved in action selection and motor control respectively.

Introduction

Life is made of decisions. Our decision-making is often influenced by our personal history. For example, reinforcement learning is a process by which decision-makers use their recent history to estimate the outcomes of different action choices for given stimuli to achieve optimal decision-making (Sutton and Barto, 1998; Lee et al., 2012). Intriguingly, history-dependence is prevalent even when the decision-makers are informed of a fixed, deterministic stimulus-action rule (e.g., 'saccade to the direction of moving dots') and thus there is no need to infer rules from history (Fründ et al., 2014; Abrahamyan et al., 2016; Braun et al., 2018). In those conditions, idiosyncratic history dependence becomes apparent when the stimuli are ambiguous and thus the sensory evidence is weak. This suggests that history-dependent decision bias is always at work, and the extent of its influence varies with the strength of sensory evidence. Thus, although its utility and impact on choice vary with the nature of decision problems, history-dependent bias is a fundamental and universal trait in decision-making.

Recent studies found that the posterior parietal cortex (PPC) is a critical locus of the neural circuit that is involved in history-dependent bias of decision-making (Hwang et al., 2017; Akrami et al., 2018). They showed that a subset of PPC neurons encode history-dependent bias and/or relevant history information, and PPC inactivation weakens history-dependent bias. These findings raise important questions pertaining to the neural circuit mediating history-dependent bias: what brain areas send inputs to PPC neurons that mediate history-dependent bias, and where PPC sends this bias information to affect choices. However, we cannot simply infer such information flows based on known anatomy given that PPC is extensively interconnected with many brain regions including sensory, motor, and other association areas (Pandya and Seltzer, 1982; Cavada and Goldman-Rakic, 1989; Baizer et al., 1993; Lewis and Essen, 2000; Hovde et al., 2018). Furthermore, PPC is involved in a diverse set of functions including decision-making, motor control, attention, object categorization, and working memory (Snyder et al., 1997; Platt and Glimcher, 1999; Shadlen and Newsome, 2001; Todd and Marois, 2004; Buschman and Miller, 2007; Freedman and Assad, 2011; Harvey et al., 2012; Hwang et al., 2012; Andersen et al., 2014; Raposo et al., 2014). Currently it remains unknown which input and output pathways of PPC contribute to each of these functions.

In one extreme scenario, the various inputs to PPC may converge indiscriminately onto all PPC projection neurons that broadcast the same information to all downstream targets. In the other extreme scenario, neurons within PPC may segregate into distinct groups with distinct input-output connectivity and functions, forming non-overlapping parallel pathways. The brain appears to utilize both of these strategies (broadcasting vs. parallel subsystems) in

different systems. A recent study on locus coeruleus noradrenergic neurons provided an example for the first scenario (Schwarz et al., 2015). In contrast, a number of other studies have shown some levels of pathway-specificity. Information encoded by neurons in a given area differs depending on their projection targets (Movshon and Newsome, 1996; Chen et al., 2013; Glickfeld et al., 2013), and perturbation of selective projection pathways can modify specific behavioral phenotypes (Tye et al., 2011; Kim et al., 2013; Li et al., 2015; Knowland et al., 2017; Murugan et al., 2017; Ren et al., 2018). It is unknown to what extent PPC has parallel subsystems, and which pathways carry out which functions.

Here, we probed these questions in order to delineate the PPC circuit underlying history-dependent decision bias. We focused on two major outputs of PPC, the dorsal striatum (STR) and the posterior secondary motor cortex (pM2). We selected these two areas as plausible downstream targets to which PPC may send bias information, because they have been implicated in action selection and preparation (Lauwereyns et al., 2002; Pasupathy and Miller, 2005; Samejima et al., 2005; Sul et al., 2011; Znamenskiy and Zador, 2013; Barthas and Kwan, 2017). We compared PPC neurons projecting to STR (PPC-STR) versus pM2 (PPC-pM2) in terms of their anatomical connectivity, response properties, and involvement during a decision-making task, using pathway-specific retrograde labelling, two-photon calcium imaging, and optogenetic inactivation. We found that PPC neurons projecting to the two targets form largely non-overlapping and parallel subpopulations, and the subpopulations that project to STR and pM2 are selectively involved in biasing action selection and controlling movements, respectively.

Results

PPC neurons projecting to STR and pM2 represent largely distinct subpopulations.

We recently established a behavioral paradigm in which the action selection of mice is biased by idiosyncratic use of their choice-outcome history. We showed that a subset of PPC neurons encode the bias information during the inter-trial interval (ITI) that predicts their subsequent action choice, and inactivation of PPC during the ITI weakens history-dependent bias. Curiously, however, PPC inactivation during the choice period had no impact on the bias (Hwang et al., 2017). These results suggested that the bias information encoded in PPC during the ITI is transferred to a downstream region where it is used during choice to bias action selection. Here we sought to identify this flow of bias information from PPC.

To examine the output connectivity of PPC, we performed anterograde tracing by injecting AAV-CAG-tdTomato in PPC unilaterally and examined its axonal projections. We found PPC projections in several brain areas, including posterior secondary motor cortex (pM2) and dorsal striatum (STR) (Figure 1A–B), as well as primary somatosensory cortex, associative thalamus, auditory cortex, visual cortex, and superior colliculus, consistent with previous reports (Harvey et al., 2012; Hovde et al., 2018). The projections were largely ipsilateral to the injection site. Of these downstream areas, we focused on STR and pM2 as plausible targets to which PPC sends action bias information, as the dorsal striatum and secondary motor cortex have been repeatedly implicated in stimulus- and history-dependent decision-making (Lauwereyns et al., 2002; Pasupathy and Miller, 2005; Samejima et al.,

2005; Sul et al., 2011; Tai et al., 2012; Znamenskiy and Zador, 2013; Hanks et al., 2015; Barthas and Kwan, 2017).

Next we examined whether the PPC projections to STR and pM2 originate from the same PPC neurons sending collaterals to both areas, or from non-overlapping subpopulations of PPC neurons, projecting to either STR or pM2 but not both. To address this question, we injected two different fluorescent retrograde tracers in each of the two targets in the same animal (Figure 1C; STAR Methods), which were taken up by axon terminals and retrogradely labeled PPC neurons (Figure 1D). The injections were targeted to the locations of dense axonal projections in the aforementioned anterograde tracing experiment (STAR Methods). In one set of mice ($N = 6$), we unilaterally injected glycoprotein-deleted rabies virus encoding GFP (RV G-GFP) in STR and RV G- tdTomato in pM2 of the same animal. In the other set ($N = 3$), we unilaterally injected cholera toxin subunit b (CTB) conjugated with Alexa Fluor 594 in STR, and CTB-Alexa-Fluor 488 in pM2. The somas of many PPC neurons were clearly labeled (Figure 1D). In mice injected with RV G, we quantified retrogradely labeled neurons in PPC of both hemispheres and found a vast majority of labeled neurons in the hemisphere ipsilateral to the injection site. The contralateral PPC contained only $2 \pm 1\%$ (mean $\pm$ S.E.M. across 6 mice) of all retrogradely labeled PPC neurons from STR injections, and $4 \pm 1\%$ from pM2 injections. Thus, the following analyses were performed only in the ipsilateral PPC.

We next examined the distributions of PPC neurons projecting to STR (PPC-STR) versus pM2 (PPC-pM2). We generally found more PPC-STR than PPC-pM2 neurons (Figure 1E). Furthermore, the two groups of PPC projection neurons showed differential spatial distributions both vertically and horizontally. To quantify the spatial distributions of labeled neurons, we constructed a relative density histogram of labeled neurons in three separate axes; dorsoventral depth from the dura, mediolateral distance from the midline, and anteroposterior distance from bregma, for each mouse. Then, we averaged the histograms across mice. As the two sets of tracers (CTB and RV G) revealed similar spatial distributions, we present combined data from the two tracers. Overall, we found a significant overlap in the spatial distributions of the two projection populations within PPC (Figure 1F). However, the two distributions were slightly offset from each other in all three axes; PPC-pM2 neurons tend to be located more superficially, laterally, and posteriorly compared to PPC-STR neurons (Figure 1F).

The different spatial distributions suggest that the two projections arise from at least partially distinct subpopulations in PPC. However, it still remains possible that some PPC neurons send axons to both STR and pM2. To characterize the degree of overlap between the two projections, we quantified the fraction of PPC neurons that were double-labeled by both STR and pM2 injections. In mice injected with RV G, we found that only $0.6 \pm 0.3\%$ (mean $\pm$ S.E.M. across 6 mice) of all labeled PPC neurons expressed both fluorescent proteins. In mice injected with CTBs, $3.5 \pm 0.1\%$ (mean $\pm$ S.E.M. across 3 mice) of all labeled PPC neurons were labeled by both fluorophores (Figure 1G). The number of CTB double-labeled neurons corresponds to $5.5 \pm 1.6\%$ of neurons labeled by CTB injected in STR (i.e., PPC-STR) and $9.2 \pm 2.2\%$ of neurons labeled by CTB injected in pM2 (i.e., PPC-pM2). The low frequency of double-labeled neurons suggests that PPC-STR and PPC-pM2 neurons

represent largely distinct subpopulations. However, we note that the two-color retrograde labeling, each with an incomplete efficiency, is likely an underestimate of the true fraction of neurons that project to both target areas. Nevertheless, together with the distinct spatial distributions, the results suggest that PPC-STR neurons and PPC-pM2 neurons are largely non-overlapping.

PPC neurons projecting to STR and pM2 receive distinct long-range inputs.

Given that we have identified two largely distinct subpopulations of PPC projection neurons, we considered the possibility that these PPC subpopulations receive distinct patterns of long-range inputs, which could contribute to potential differences in their activity and functions. Thus, we characterized long-range inputs to PPC-STR and PPC-pM2 neurons using projection-specific, retrograde monosynaptic labeling (Schwarz et al., 2015; Knowland et al., 2017). Briefly, we first injected a Cre-encoding retrograde canine adenovirus (CAV-Cre) in one of the two targets and a mixture of helper viruses (AAV-DIO-mRuby2-P2A-TVA and AAV-DIO-RVG) in PPC unilaterally. This strategy restricts helper virus expression to the specific subset of PPC neurons that project to either STR or pM2: starter neurons. Three weeks after these first injections, we injected EnvA-pseudotyped, glycoprotein-deleted rabies virus (EnvA-RV G-eGFP) in PPC (Figure 2A; N = 5 mice for each target; STAR Methods). This rabies virus variant can only infect starter neurons, where trans-complementation enables it to trans-synaptically infect their pre-synaptic neurons (Wickersham et al., 2007). Similar to the pattern of long-range inputs to the general PPC population (Harvey et al., 2012; Hovde et al., 2018), we found inputs to each projection group from numerous cortical areas and associative thalamic nuclei, mostly in the ipsilateral hemisphere of the injections. The number of contralateral inputs corresponds to $6 \pm 1\%$ (mean $\pm$ S.E.M. across 10 mice) of total inputs, and the fraction of contralateral inputs did not significantly differ between the two projection groups (bootstrap two-sample (BTS) test, p=0.6). We focused our analysis on inputs from 19 dorsal cortical areas in the hemisphere ipsilateral to the injections. These areas include somatosensory, visual, cingulate, retrosplenial, and motor cortical areas and the 19 areas together comprised $77 \pm 3\%$ (mean $\pm$ S.E.M. across 10 mice; STAR Methods) of total input neurons. While both projection groups received inputs from all of these areas, the relative proportions of inputs from these areas were differently distributed between the two projection groups (Figure 2B–C). PPC-pM2 neurons received more inputs from the primary motor cortex and the primary somatosensory upper-body regions (i.e., forelimb, trunk, shoulder, and neck regions) than PPC-STR neurons (BTS test, p<0.0001 and p<0.001, respectively; Figure 2D). In contrast, PPC-STR neurons received more inputs from the cingulate areas, i.e, cingulate cortex areas 1 and 2, and cingulate/retrosplenial complex (transitional zone between cingulate and retrosplenial cortex) than PPC-pM2 neurons (BTS test, p<0.0005; Figure 2D). Therefore, the distinct subpopulations of PPC neurons, each projecting to STR or pM2, receive different distributions of long-range cortical inputs. Sensorimotor inputs appear enriched in PPC-pM2 neurons, while association inputs are more prevalent in PPC-STR neurons.

History-dependent bias is preferentially encoded by PPC neurons projecting to STR.

The results that PPC-STR and PPC-pM2 neurons are largely non-overlapping and receive distinct input patterns suggest that the two projection pathways may form parallel

subsystems with distinct functions. Specifically, we asked whether the PPC function of mediating history-dependent action bias preferentially involves one of these subpopulations. To address this issue, we first examined information encoded by the two subpopulations of PPC projection neurons during a decision-making task (Figure 3A).

In this task (Hwang et al., 2017), mice were presented with one of two visual stimuli (forward or downward drifting gratings) for 1 sec in each trial. Two seconds after the stimulus offset, an auditory go cue indicated that mice must press the joystick in the same direction as the visual stimulus presented earlier, to receive a water reward. We previously found that a significant portion of choice variability in this task was explained by choice-outcome history-dependent bias (Hwang et al., 2017). Following our previous methods, we quantified choice-outcome history dependence in this task by modeling the choice behavior. Briefly, we built a logistic regression model in which the probability to choose one of the two alternatives on a given trial (N) is a function of the current trial stimulus, choice-outcome history, and a constant bias (full model, Equation 1), and we fit the weights of this logistic regression model in each session based on the choice pattern (STAR Methods).

$$\log \frac{p\{choice(N) = forward\}}{p\{choice(N) = downward\}} = w_s \cdot stimulus(N) + w_o \cdot \sum_{k=1}^{N-1} outcome(k)$$

$$\cdot\, e^{\frac{N-1-k}{\tau_o}} + w_c \cdot \sum_{k=1}^{N-1} choice(k) \cdot e^{-\frac{N-1-k}{\tau_c}} + w_{oc} \cdot \sum_{k=1}^{N-1} outcome(k) \cdot choice(k) \quad (1)$$

$$\cdot\, e^{-\frac{N-1-k}{\tau_{oc}}} + constant$$

Each term in the model can account for distinct behavioral strategies/tendencies. For instance, a positive w_s would reproduce a tendency for the animal to use the correct stimulus-response rule. w_o would be positive if the animal tends to choose "forward" after rewarded trials, but "downward" after failed trials. w_c would be negative if the animal tends to choose the less chosen option in the recent history. A positive w_{oc} would indicate a tendency that the animal repeats the rewarded choices independent of the stimulus (e.g. a win-stay/lose-switch strategy). The relative strength of each tendency in the animal's choices would be reflected on the amplitude of their corresponding weight. We used exponential decay for each of the history terms based on a pilot analysis, which showed that the effects of history from previous trials decay in an approximately exponential manner (not shown). In general, the behavioral data in the current study (51 sessions across 13 mice) replicated the main findings in our previous publication (Hwang et al., 2017). First, the outcome history has the strongest effect on choices in a majority of sessions (28/51). Second, the effect of the outcome history is dominated by N-1 trial with a short time constant (0.6 ± 0.2 trials; median $\pm$ S.E. across 51 sessions), Third, the choice history has a significantly negative weight (-0.3 ± 0.06; mean $\pm$ S.E.M.; bootstrap paired-sample (BPS) test, p<0.0001) with a longer time constant (17 ± 8 trials; median $\pm$ S.E.) than the outcome history.

This 'full model' predicted the animals' choice in a cross-validated condition significantly better than the 'stimulus model' (Equation 2) that uses only the stimulus and constant (BPS test, p<0.0001; Figure 3B).

$$\log\frac{p\{choice(N) = forward\}}{p\{choice(N) = downward\}} = w_s \cdot stimulus(N) + constant \tag{2}$$

The higher performance of the full model with the history terms was also confirmed by the Akaike information criterion (AIC) that penalizes an increase in the number of parameters, with significantly better (smaller) AIC for the full model (BPS test, p<0.0001; Figure 3C). Each mouse performed multiple sessions, so we also examined the average model performance and AIC for each mouse and observed the same trend (Figure 3B–C).

This model has two important implications. First, the result confirms significant dependence on choice-outcome history in the two-choice joystick task. Second, by fitting the full model to the observed choices, we could estimate the continuously-varying history-dependent bias on a trial-by-trial basis, which is a variable internal to the mouse and not directly measurable. More specifically, once the weights of the full model are identified from fitting, the portion of the full model excluding the stimulus term (Equation 3) could provide an estimate of history-dependent bias in each trial. This estimate of choice-outcome history-dependent bias will be referred to as "history bias" hereafter. In the following experiments, we sought to identify neural correlates of this history bias in PPC.

$$History\ bias\ (N) = w_o \cdot \sum_{k=1}^{N-1} outcome(k) \cdot e^{-\frac{N-1-k}{\tau_o}} + w_c \cdot \sum_{k=1}^{N-1} choice(k)$$

$$\cdot e^{-\frac{N-1-k}{\tau_c}} + w_{oc} \cdot \sum_{k=1}^{N-1} outcome(k) \cdot choice(k) \cdot e^{-\frac{N-1-k}{\tau_{oc}}} + constant \tag{3}$$

To record the activity of specific projection neurons and compare it to the activity of other PPC neurons, we combined retrograde labeling (described later) and two-photon calcium imaging in transgenic mice (*CaMK2a-tTA::*tetO-GCaMP6s or *CaMK2a-tTA::tetO-GcaMP6s::Rosa-CAG-LSL-tdTom*) in which cortical excitatory neurons express GcaMP6s (STAR Methods). Our previous study (Hwang et al., 2017) demonstrated that the general population of PPC neurons reflects history bias for the upcoming choice during the ITI. Consistent with this previous finding, we found that $24 \pm 2\%$ (mean $\pm$ S.E.M. across 51 PPC fields in 13 mice, 1 session / field) of all imaged PPC neurons exhibited significantly different activity during the ITI depending on the upcoming choice (i.e., N-choice tuning; Figure 3D), suggesting that these neurons reflect the internal bias that influences the upcoming choice. In addition, a weighted sum of ITI activity across PPC neurons in each trial could well reflect the history bias of that trial in the model, closely fitting the history bias that varies trial-by-trial (Figure 3E; Equation 6 in STAR methods; $r = 0.5 \pm 0.03$, mean $\pm$ S.E.M. across 51 sessions, cross-validated). Therefore, our current dataset reproduced our previous finding that the ITI activity in PPC represents the history bias (Hwang et al., 2017).

Having established the representation of history bias in the general population of PPC neurons, we examined whether PPC-STR and PPC-pM2 neurons encode the bias information differently from each other and/or from the general population. Projection neurons were labeled with tdTomato as we injected retrograde CAV-Cre in either STR (N = 5 mice) or pM2 (N = 8 mice) before behavioral training began. In the case of CaMK2-tTA::tetO-GcaMP6s, we made a second injection of AAV-CAG-FLEX-tdTomato in PPC (Figure 4A; STAR Methods). Of the projection neurons that were retrogradely labeled, 47 ± 3% (mean ± S.E.M. across 51 PPC fields) showed detectable GCaMP6s signals. Using this method, we examined the activity of PPC-STR neurons (N = 1,322 from 26 imaging fields in 5 mice), PPC-pM2 neurons (N = 465 from 25 fields in 8 mice), and those that were not labeled by tdTomato (N = 11,702 neurons from 51 fields in 13 mice). In the mice where PPC-pM2 or PPC-STR neurons are labeled respectively, the unlabeled neurons should include neurons that project to the opposite target (STR or pM2) or neither target, and a fraction of neurons that project to pM2 or STR that did not get labeled. We chose the fields of view with a high density of tdTomato neurons in each mouse. As a result, PPC-STR neurons tended to be imaged from deeper fields than PPC-pM2 neurons (Figure 4B), consistent with the histological assay in our two-target retrograde tracing experiment (Figure 1F). Overall, in our imaging fields, PPC-STR neurons tended to be denser than PPC-pM2 neurons (Figure 4C). Mice in the two labeling groups (PPC-STR vs. PPC-pM2) showed similar history dependence and task performance (Figure S1).

To compare bias information coding among three types of neurons (PPC-STR, PPC-pM2, and unlabeled), we first pooled neurons across sessions for each type and computed the fractions of N-choice tuning during the ITI. We found that N-choice tuning was substantially more prevalent in PPC-STR neurons than in the unlabeled or PPC-pM2 neurons, and less prevalent in PPC-pM2 neurons than in the unlabeled neurons (χ^2 test, p<0.0005 in all comparisons; Figure 4D). The differences between the neuron groups were also robustly observed within individual sessions (Figure 4E, 1 imaging field/session). That is, PPC-STR neurons were more likely tuned to N choice than unlabeled neurons within individual sessions (BPS test, p<0.04), while PPC-pM2 neurons were less likely tuned to N choice than unlabeled neurons within individual sessions (BPS test, p<0.03).

Given that PPC-STR neurons tended to be imaged from deeper fields (Figure 4B), we asked whether N-choice tuning of PPC neurons increases with depth in general. To answer this question, we examined correlation between the depth of imaging field and the fraction of neurons tuned to N choice in all imaged neurons in each field (i.e., all neurons expressing GCaMP6s in each field). Across 42 sessions in which we recorded the depth of imaging field, we found a significantly positive correlation that the fraction of neurons tuned to N choice increases with depth (Pearson's correlation coefficient, r = 0.6, p<1e-5). This depth-dependent tuning within PPC raises a possibility that different N-choice tuning between PPC-STR and PPC-pM2 populations might be solely explained by the difference in their depths. To test this possibility, we analyzed a subset of imaging fields acquired at similar depths (250–350 μm) between the two projection groups (9 sessions per group; Figure 4F). When the depths were matched, the fraction of neurons tuned to N choice in all imaged neurons in each field was not different between the two groups (Figure 4G). However, the fraction of neurons tuned to N choice was still significantly larger in PPC-STR than PPC-

pM2 or unlabeled neurons even in this depth-matched comparison (Figure 4H and Figure S2). This result indicates that differences in choice information coding between the two projection groups cannot be fully explained by the difference in their depths.

Notably, significant tuning to N choice could reflect the encoding of the continuously-varying history bias as suggested earlier, or the encoding of the binary choice. To separate tuning to these related variables, we applied a multiple linear regression on the ITI activity using N choice and the history bias estimated from the full model (Equation 3) as predictors (STAR Methods), and compared the fraction of neurons with a significant weight for each predictor. Supporting the notion that PPC encodes history bias, the fraction of neurons with a significant weight for the history bias was significantly higher than the fraction with a significant weight for N choice in all neuronal groups (χ^2 test, p<0.0001 in all three comparisons; Figure 4I). Moreover, the fraction of neurons with a significant weight for the history bias was significantly higher in PPC-STR than PPC-pM2 and unlabeled neurons (χ^2 test, p<0.0001 in both comparisons; Figure 4I). As shown in Equation 3, the history bias arises from three types of history: outcome, choice, and outcome-choice interaction. To examine the coding of each of the three bias components, we performed a similar multiple linear regression replacing the history bias with its three separate bias terms. We found that, in all three populations of neurons, the fraction of neurons with a significant weight was significantly larger for the outcome history bias than the choice history bias or interaction history bias (χ^2 test, p<0.0001 in all six comparisons; Figure S3). Furthermore, for both the outcome history bias and choice history bias, the PPC-STR population contained a significantly higher fraction of neurons with a significant weight than the PPC-pM2 population (χ^2 test, p<0.05 in both comparisons; Figure S3).

We next evaluated history bias coding at the population level. As shown earlier, the history bias that varies trial-by-trial is well represented by a linear sum of the ITI activity of neurons in the general PPC population (Figure 3E). Therefore, to compare history bias coding at the population level, we computed how well a linear sum of the activity of individual neurons in the three groups can fit the history bias on a trial-by-trial basis (Equation 6, STAR methods). This analysis revealed that the population activity of PPC-STR neurons reflected the history bias better than unlabeled and PPC-pM2 neurons (BTS test for the average across sample sizes, p<0.02 and p<0.0001, respectively; Figure 4J). A better coding of the history bias by the PPC-STR population was also confirmed in other, non-linear decoding methods (Figure S4; STAR Methods). Taken together, the history bias information is preferentially represented in the PPC-STR population than the other two subpopulations, suggesting that the PPC may bias action selection via its STR projection pathway.

PPC-STR pathway is required for history bias.

Our finding that history bias is preferentially encoded in the PPC-STR population predicts that perturbing the activity of PPC-STR neurons might alter the history dependence of choice. To test this prediction, we performed inactivation of PPC-STR neurons and examined its effects on choice behavior. The PPC-STR neuron-specific inactivation was achieved by injecting CAV-Cre in STR and AAV encoding the light-dependent chloride pump, halorhodopsin, in a Cre-dependent manner (AAV-EF1a-DIO-eNpHR3.0-eYFP) in

PPC (N = 7 mice; Figure 5A). Both injections were performed bilaterally. Inactivation experiments were carried out at least 8 weeks after the injections to ensure high expression levels of the opsin. Inactivation was performed in 15% of randomly selected trials (light-on), by shining green light on the cranial windows over PPC bilaterally during the ITI (Figure 5B). To inspect whether history dependence was affected by inactivation, we used the aforementioned behavioral models. First, we fit the full model (Equation 1) and stimulus model (Equation 2) separately to the observed choices (both 10-fold cross-validated). Then, we estimated history dependence as the difference of choice prediction accuracy between the two models:

$$History\ dependence = full\ model\ accuracy - stimulus\ model\ accuracy$$

The rationale is that any additional choice variability explained by the full model is attributable to the history terms in the full model. In the inactivation experiment, we measured history dependence separately for inactivation (light-on) and control (light-off) trials (number of trials were matched; STAR methods). If history bias is mediated by PPC-STR neurons, inactivating them would decrease history dependence in animals' choices.

Indeed, we found that history dependence was significantly weaker in light-on than light-off trials (BPS test, p<0.0001; Figure 5C). The decreased history dependence was not due to non-specific effects of light, as the green light applied over the head bar in the same mice did not affect history dependence (BPS test, p=0.12; Figure 5C). Thus, the activity of PPC-STR neurons is required for normal history dependence in our task.

We next examined the specificity of this effect by performing an analogous inactivation experiment on PPC-pM2 neurons (N = 8 mice; STAR Methods). In contrast to the PPC-STR inactivation, history dependence was not significantly affected by inactivating PPC-pM2 neurons (BPS test, p=0.38; Figure 5D). Thus, the activity of PPC-pM2 neurons is not required for normal history dependence. Furthermore, this experiment serves as a control for non-specific effects of light within PPC, such as heating. These results suggest that PPC-STR neurons are selectively involved in controlling history bias.

PPC-STR neurons may mediate history bias through their projection to STR. Alternatively, the bias may be mediated by axon collaterals of these neurons to other downstream targets and projections to STR may not be important for the bias. To distinguish these possibilities, we performed a projection-terminal inactivation experiment. We expressed halorhodopsin selectively in PPC-STR neurons bilaterally in the same way as the soma inactivation experiment described above. We then implanted fiber optic cannulae in STR bilaterally, targeting the area within STR that receives dense projections from PPC (STAR Methods), to inactivate the projection terminals in STR (N = 7 mice; Figure 5E). We found that, similar to soma inactivation, inactivation of the terminals of PPC-STR neurons in STR significantly decreased history dependence (BPS test, p<0.0005; Figure 5F). The significant effect is not due to non-specific effects such as heating, as a delivery of light to STR in the absence of halorhodopsin did not affect history dependence in a consistent way (Figure 5E–F). Therefore, inactivating PPC-STR neurons, both soma and terminal, but not PPC-pM2 neurons, lead to a significant decrease in history dependence. Direct comparisons across

experiments revealed that the effect sizes in soma and terminal inactivation of PPC-STR neurons were significantly larger than that of PPC-pM2 soma inactivation (BTS test, p<0.05 in both comparisons; Figure 5G). The effect sizes of PPC-STR neuron soma inactivation and terminal inactivation were not significantly different (p=0.98; Figure 5G).

In another analysis, we assessed history dependence using a third behavioral model, history model, in which choices are predicted from choice-outcome history terms without stimulus (Equation 4, STAR Methods), following the methods we used in our previous publication (Hwang et al., 2017). This analysis also revealed the same finding that history dependence is significantly altered only in PPC-STR soma and terminal inactivation (Figure S5A–C; STAR Methods). It is also noteworthy that the effect size of inactivation specific to the PPC-STR neurons, both soma and terminal, is similar to what we observed when we inactivated the entire PPC in our previous publication by activating parvalbumin-positive inhibitory neurons (Figure S5D) (Hwang et al., 2017), further highlighting the importance of the PPC-STR pathway in controlling history bias.

Taken together, these results consistently indicate that PPC controls the history bias in our decision-making task via its projections to STR. Thus, the bias information encoded in PPC during the ITI might be offloaded to the basal ganglia where it is used to bias action selection.

PPC-pM2 neurons are involved in movement control.

The results above suggest that history dependence is controlled selectively by the PPC-STR pathway. An intriguing remaining question is which PPC functions require PPC-pM2 neurons. Studies of humans and non-human primates reported that PPC is also important for the control of reaching movements (Pisella et al., 2000; Hwang et al., 2012, 2014; Andersen et al., 2014). The stronger inputs from sensorimotor areas to PPC-pM2 neurons observed in our long-range input assay (Figure 2) suggest that PPC-pM2 pathway might be involved in the control of movements. To test this possibility, we examined how kinematic features of movements in our task were affected in the three inactivation experiments described above. We found that task performance (i.e. fraction of correct choice) did not change significantly in any of the inactivation conditions (Figure S6). However, the similarity of movements from trial to trial was significantly reduced by inactivating PPC-pM2 neurons (Figure 6A). This effect was not observed in control or PPC-STR inactivation sessions, both soma and terminal (Figure 6A–C). In addition, the peak velocity of movements was slightly but significantly reduced by inactivating PPC-pM2 neurons, but not PPC-STR somas or terminals (Figure 6D). These kinematic changes from inactivation of PPC-pM2 during ITI suggest that PPC-pM2 neurons might contribute to the preparation of movements to produce faster and consistent movements.

Discussion

We found that PPC-STR and PPC-pM2 neurons form distinct subpopulations and receive different patterns of long-range cortical inputs. Furthermore, PPC-STR neurons encode history bias more strongly than unlabeled and PPC-pM2 neurons, and inactivating PPC-STR neurons, but not PPC-pM2, weakens history bias. In contrast, inactivating PPC-pM2

neurons, but not PPC-STR neurons, alters movement kinematics. These results suggest that PPC controls different functions through different projection pathways; history-dependent bias in decision-making via its projections to STR, and kinematic control of movements via its projection to pM2 (Figure 7).

We found that PPC-STR and PPC-pM2 neurons receive long-range inputs from similar cortical areas, but the proportions of inputs were different. These results suggest that these two PPC subpopulations form partially distinct, parallel input-output pathways. Similar to our finding, several subcortical areas that mediate diverse behavioral effects contain parallel projection pathways, each associated with a distinguishable pattern of long-range inputs (Lammel et al., 2012; Wall et al., 2013; Knowland et al., 2017; Ren et al., 2018). However, differences in long-range inputs may not be the only cause underlying the different bias coding between the two PPC projection populations. Neural processing within PPC microcircuitry likely amplifies the different long-range inputs that these projection neurons receive. Furthermore, it has been found that neurons projecting to different targets can display distinguishable genetic phenotypes (Murugan et al., 2017; Economo et al., 2018; Ren et al., 2018). Thus, distinct intrinsic properties of neurons comprising each subpopulation may also contribute to the functional differences between the pathways.

Our results do not exclude the possibility that other output pathways in PPC that are not tested in this study might also be necessary for controlling history bias. Nevertheless, inactivation of PPC-STR terminals in STR weakened history bias as much as inactivation of all PPC neurons, suggesting that the PPC-STR pathway is critical for history bias. We acknowledge that optogenetic inactivation of axon terminals is challenging and inhibitory opsins can sometimes facilitate neurotransmitter release (Mahn et al., 2016; Messier et al., 2018). One of these studies recommended the use of halorhodopsin for terminal inactivation as no facilitating effects were observed (Mahn et al., 2016). Thus, we chose to use halorhodopsin for our terminal inactivation experiment. Regardless, however, the ultimate purpose of our terminal inactivation experiment was to perturb the normal pattern of activity of the PPC-STR pathway, and an artificial and non-specific decrease or increase of neurotransmitter release would both serve this purpose.

The involvement of the PPC-STR pathway in history bias fits well with previous findings regarding STR. First, sensorimotor associative learning can modify synaptic strengths between sensory cortical neurons and dorsal striatal neurons (Znamenskiy and Zador, 2013; Xiong et al., 2015). Such plasticity can generate a learned stimulus-response map by which sensory inputs can drive associated responses. The stimulus-response map would be an ideal locus at which history-dependent information biases sensory-guided choices. Second, dorsal striatal neurons encode the reward history-dependent action value (Samejima et al., 2005), and transient optogenetic stimulation of dorsal striatal neurons during a decision-making period can bias reward history-dependent choices (Tai et al., 2012). Therefore, STR appears to be a part of the circuit that biases choices in a history-dependent manner. Third, striatal neurons tuned to a particular action show elevated pretrial activity when the neuron's preferred action is associated with a higher reward (Lauwereyns et al., 2002). In this case, the animals are presumably biased towards the action with a higher reward, so the pretrial activity modulation in striatal neurons may be reflective of history bias that the STR receives

from PPC inputs. Taken together, a compelling idea is that sensory-driven action selection in STR might be influenced by history bias transmitted from PPC, and such an interaction between PPC and STR may give rise to complex history dependence in sensory-guided decision-making tasks (Busse et al., 2011; Abrahamyan et al., 2016; Hwang et al., 2017; Akrami et al., 2018).

We found that inactivation of PPC-pM2 neurons alters movement kinematics, resonating well with our anatomical result that PPC-pM2 neurons receive stronger inputs from sensorimotor areas compared to PPC-STR neurons. It is also compatible with the previous reports in humans and non-human primates that inactivating PPC or lesions in PPC disturb reaching movements (Desmurget et al., 1999; Andersen et al., 2014). These studies suggested that PPC is involved in both planning and online adjustment of movements. The kinematic changes induced by our ITI inactivation might be related to the function of movement planning. The ITI activity of PPC-pM2 neurons might be used to prime pM2 and/or its connected motor cortex to form preparatory activity for a movement, likely the one associated with the choice bias. Given that preparatory activity in motor cortex encodes various kinematic features of upcoming movements such as the reaching movement direction, amplitude, and velocity (Crammond and Kalaska, 1994; Churchland et al., 2006; Guo et al., 2014), the PPC-pM2 pathway may be critical for the formation of proper preparatory activity in the downstream motor areas to ensure normal movement speed and consistency.

In summary, we conclude that the PPC-STR pathway is selectively involved in biasing action selection and PPC-pM2 neurons in the control of movements. We propose that PPC may control a wide range of behavioral functions by operating within-region subsystems in parallel, each with distinct patterns of input-output connectivity.

STAR Methods

LEAD CONTACT AND MATERIALS AVAILABILITY

Further information and requests for resources and reagents should be directed to the Lead Contact, Takaki Komiyama (tkomiyama@ucsd.edu).

EXPERIMENTAL MODEL AND SUBJECT DETAILS

All procedures were in accordance with protocols approved by the UCSD Institutional Animal Care and Use Committee and guidelines of the National Institute of Health. Mice (both male and female, at least 6 weeks old; anatomical tracing: *wildtype C57BL/6*, Charles River Laboratories; calcium imaging: triple cross between *B6.Cg-Gt(ROSA)26Sor^{tm14(CAG-tdTomato)Hze}/J* [JAX 007914; also known as *Rosa26-CAG-LSL-tdTomato*], *B6.CBA-Tg(Camk2a-tTA)1Mmay/J* [JAX 003010; also known as *Camk2a-tTA*], and *B6.DBA-Tg(tetO-GCaMP6s)2Niell/J* [JAX 024742; also known as *tetO-GCaMP6s*] or cross between *Camk2a-tTA* and *tetO-GCaMP6s*; optogenetic perturbation: *wildtype C57BL/6* or *Rosa26-CAG-LSL-tdTomato*) were housed in a room with a reversed light cycle (12 h–12 h). Experiments were performed during the dark period. We performed

experiments in both male and female subjects, but did not perform sex-specific analyses as both types were randomly assigned to all experimental groups that we compared.

METHOD DETAILS

Virus production—AAV-EF1α-DIO-mRuby2-P2A-TVA and AAV-EF1α-DIO-RVG were packaged as serotype DJ and generated as previously described (Lim et al., 2012; Knowland et al., 2017). In brief, AAV vectors were produced by transfection of AAV293 cells (Agilent) with three plasmids: an AAV vector plasmid carrying target constructs (DIO-mRuby2-P2A-TVA, DIO-RVG), AAV helper plasmid (pHELPER; Agilent), and AAV rep-cap helper plasmid (pRC-DJ). At 72 hr post-transfection, the cells were collected and lysed by a repeated freeze-thaw procedure. Viral particles were then purified by an iodixanol step-gradient ultracentrifugation and subsequently concentrated using a 100-kDa molecular cutoff ultrafiltration device (Millipore). The genomic titer was determined by quantitative PCR. The AAV vectors were diluted in PBS to a working concentration of approximately 10^{12} - 10^{13} genomic copies/ml.

Rabies viruses were designed and generated as previously described (Osakada and Callaway, 2013; Knowland et al., 2017). In brief, B7GG cells were transfected with a total of five plasmids: four plasmids expressing the viral components pcDNA-SADB16N, pcDNA-SADB16P, pcDNA-SADB16L, pcDNA-SADB16G and the rabies virus genomic vector carrying eGFP or tdTomato coding sequence. The virus-containing media was collected 3–4 days post-transfection and used for further amplification. Viral particles were harvested from the media by centrifugation using SureSpin630 rotor at 20,000 rpm for 2 hr. Rabies viral particles were reconstituted from the pellets with PBS and immediately stored at - 80 °C. To generate EnvA-pseudotyped, glycoprotein-deleted rabies virus expressing eGFP (EnvA-RV G-eGFP), we used a modified version of a published protocol (Osakada and Callaway, 2013).

Anterograde tracing—For anterograde tracing, mice (*wildtype C57BL/6*) were injected with 20 nL of virus encoding tdTomato (AAV1-CAG-tdTomato; UPenn Vector Core) in the right PPC (1.7 mm lateral, 2.0 mm posterior, 0.35 mm beneath the dura). In 10–14 days, the mice were perfused transcardially with PBS followed by paraformaldehyde solution (PFA, 4%). The brain was carefully removed from the skull and stored in 4% PFA solution for a day and subsequently in 30% sucrose solution for 1–3 days at 4 °C. The brain was then cut in 60 m coronal sections on a freezing microtome throughout the anterior-posterior axis (+2.8 to −4.2 mm from bregma). The sections were mounted on Superfrost Plus microscope slides (Fisher Scientific) with CC/Mount mounting medium (Diagnostic Biosystems). To visualize the fluorescent axons projecting from PPC, the mounted slides were manually imaged using a Zeiss Axio Zoom microscope.

Retrograde tracing—For two-target retrograde tracing, wildtype mice were placed in a stereotaxic frame and retrograde tracers were injected in the right STR (2.2 mm lateral, 0.8 mm posterior to bregma, 2.3 mm beneath the dura) and the right pM2 (0.5 mm lateral, 0.3 mm anterior to bregma, 0.35 mm beneath the dura) through bur holes. In one set of mice (N = 6), we injected 100 nL of RV G-GFP in STR and 100 nL of RV G-tdTomato in pM2. In

the other set (N = 3), we injected 500 nL of CTB-Alexa-Fluor 594 in STR, and 500 nL of CTB-Alexa-Fluor 488 in pM2. The coordinates of STR and pM2 were selected to target the areas showing the densest projections from PPC as identified in the anterograde tracing experiment. After a week, the mice were perfused and their brains were prepared as described above. 60 μm coronal sections containing PPC (1.8–2.2 mm posterior to bregma) were mounted on Superfrost Plus slides with CC/Mount mounting medium. Brain slices expressing fluorescent proteins encoded by RV-DG were imaged using a Zeiss Axio Zoom microscope, and brain slices with CTB labeling were imaged using an Olympus FluoView FV1200 confocal microscope. The number of somas expressing GFP and/or tdTomato were manually counted. When counting somas labeled with CTB-Alexa Flours, we first used an ImageJ (Schneider et al., 2012) tool *find maxima* to automatically detect cell bodies with fluorescent signals distinguishable from the background, and then manually corrected false or missed detections by visual inspection. Counting was performed within PPC, spanning 1.8–2.2 mm posterior to bregma and 1.0–2.7 mm from the midline.

Projection-specific monosynaptic retrograde tracing—For projection-specific monosynaptic retrograde tracing, we adapted the previously published protocol (Schwarz et al., 2015; Knowland et al., 2017). Wildtype mice were placed in a stereotaxic frame and Cre-encoding canine adenovirus (CAV-Cre, 150 nL; BioCampus) was injected in either the right STR or pM2 through a bur hole. When injecting CAV-Cre in STR, we performed the following procedure to minimize virus leakage and backflow in the brain areas above STR. We first back-filled a glass pipette (~30 μm outer diameter at the tip) with mineral oil, and then we front-filled the pipette tip with 150 nL of CAV-Cre followed by 10 nL of mineral oil by retracting the pipette plunger using a hydraulic manipulator (Narishige). The mineral oil at the tip provides a seal of the tip to prevent virus leakage during the advancement of the tip towards the target. We advanced the pipette past the target by ~500 μm and unloaded the mineral oil. After retracting back to the target, we unloaded the virus slowly over ~15 minutes, after which the pipette was not moved for 20 minutes allowing the virus to spread in the target region. When retracting the pipette out of the brain, we stopped every 200 μm and injected 5 nL of mineral oil to prevent backflow of the virus.

On the same or the following day of CAV-Cre injection, 1:1 mixture of AAV-DJ-EF1α-DIO-mRuby2-P2A-TVA and AAV-DJ-EF1α-DIO-RVG was injected in the right PPC through a bur hole (100 nL, each at a depth of 250 μm and 650 μm). In three weeks after the AAV injection, EnvA-pseudotyped, glycoprotein-deleted rabies virus (EnvA-RV G-eGFP, 150 nL, each at a depth of 250 μm 650 μm) was injected in the right PPC. After a week, mice were perfused and prepared as described above for histological analysis.

Each brain was cut in 60 μm coronal sections on a freezing microtome throughout the anterior-posterior axis (+2.8 to −4.2 mm from bregma). The sections were mounted on Superfrost Plus microscope slides with DAPI Fluoromount-G mounting medium (SouthernBiotech). The mounted slides were loaded to an Olympus VS120 slide scanner to visualize fluorescent cells. In brief, this process first obtained a brightfield overview image. Regions of interest were manually drawn over each section and focused with 5 focal points per region. For each section, 3 channels were obtained sequentially for DAPI, eGFP and mRuby2. Exposure times were independently adjusted to maximize signal to noise ratio.

After image acquisition, the display intensity for each section for each channel was manually adjusted to clearly identify single cells. We attempted to identify the starter neurons, which should express both eGFP and mRuby2. However, we observed very few double-positive neurons, which we speculate might be due to a competition of the two viral vectors when infecting the same neurons.

As labeled somas were found predominantly in the right hemisphere (i.e., ipsilateral to injections), we performed our manual mapping analysis only for the inputs from the ipsilateral hemisphere, based on the mouse brain atlas (Paxinos and Franklin, 2004). We focused our long-range input analysis on 19 dorsal cortical areas, which were clustered into 8 subgroups as follows: 1) primary motor cortex, 2) secondary motor cortex, 3) primary somatosensory area (S1) upper-body regions: S1 forelimb region, S1 trunk region, S1 shoulder region, and S1 shoulder/neck region, 4) S1 hindlimb region, 5) all other primary somatosensory area: unassigned S1, S1 barrel region, and S1 dysgranular region, 6) cingulate area: cingulate cortex area1, cingulate cortex area2, and cingulate/retrosplenial complex (transitional zone between cingulate and retrospleninal cortex), 7) retrosplenial area: retrosplenial granular cortex, and retrosplenial agranular cortex, 8) visual area: primary visual cortex, secondary visual cortex (V2) mediomedial area, V2 mediolateral area, and V2 lateral area. Neuron counts were normalized as a fraction of the total number of green fluorescent neurons from both hemispheres in each brain, including those that were not in the 19 areas analyzed in detail.

Two-choice joystick task—Prior to imaging or inactivation experiments, mice were trained under head-fixation in the behavioral apparatus, approximately 1 hour per day over a period of 2–4 months. The two-choice joystick task was gradually shaped through multiple training steps similar to the procedures described in our previous study (Hwang et al., 2017). In the two-choice task, in each trial, one of two visual stimuli (forward or downward drifting gratings) was presented for 1 sec. Two seconds after the stimulus offset, an auditory tone ('go' cue) was played to mark the answer period. At the same time, the joystick was released from the electromagnetic immobilization at the origin so that mice could press and move it away from the origin. Mice must press the joystick at least 6 mm away from the origin, within 10 sec from the go cue, in the same direction as the visual stimulus presented earlier, to receive a water reward. The visual stimulus was randomly selected between forward or downward drifting gratings with the following constraints: 1) after three consecutive rewarded trials in one direction, the stimulus always switched to the other direction, and 2) after error trials, the same stimulus was repeated.

Behavioral model—We used three variants of behavioral models to predict the choices of our mice; full model, stimulus model, and history model. In the full model, the choice on a given trial (N) is predicted by a weighted sum of the current stimulus (forward or downward), the history of past trial outcome (reward or not), choice (forward or downward), and their interaction, and a constant (Equation 1). Past trials were temporally discounted with an exponential decay (i.e. stronger effect from more recent trials) with time constants fit independently for each history variable. Stimulus, outcome, and choice were all binary variables with the value of 1 or −1. However, in trials in which mice did not reach any target,

choice and outcome were set to 0 (no choice) and −1 (no reward), respectively. In the stimulus model, choice probability depends only on the current trial stimulus and a constant (Equation 2). In the history model, choice probability depends on the choice-outcome history and a constant, but not stimulus (Equation 4).

$$
\log\frac{p\{choice(N) = forward\}}{p\{choice(N) = downward\}} = w_o \cdot \sum_{k=1}^{N-1} outcome(k) \cdot e^{-\frac{N-1-k}{\tau_o}} + w_c
$$
$$
\cdot \sum_{k=1}^{N-1} choice(k) \cdot e^{-\frac{N-1-k}{\tau_c}} + w_{oc} \cdot \sum_{k=1}^{N-1} outcome(k) \cdot choice(k) \tag{4}
$$
$$
\cdot e^{\frac{N-1-k}{\tau_{oc}}} + constant
$$

We modified our previous methods (Hwang et al., 2017) to more rigorously estimate the model weights and time constants. Instead of using a grid search on time constants, we computed both time constants and weights based on maximum likelihood estimation using a Matlab nonlinear optimization function, *fmincon*. The objective function was a negative log-likelihood that model parameters (i.e., weights and time constants) produce the observed choices, and the time constants were constrained to be nonnegative. To avoid settling at local optima, we performed searches multiple times from 12 initial conditions in which the initial weights were set to be 0, 1, 30, or 100, and the initial time constants were 0.01, 50 or 100. The 12 searches resulted in 12 sets of model parameters (i.e., weights and time constants) and their associated log-likelihood. Of these 12 parameter sets, we used the one associated with the maximum log-likelihood. The performance of this model was 10-fold cross-validated. That is, trials within a session were divided in 10 non-overlapping parts, where each part served as a test set once, and the other nine parts as a training set. The fit of the model (or simply, model accuracy) was measured as the fraction of test trials in which the estimated choice (Equation 5) matched the actual choice.

$$
\widehat{choice}(N) = \left.\begin{array}{ll} 1, & if\ p\{choice(N) = forward)\} > 0.5 \\ -1, & otherwise \end{array}\right\} \tag{5}
$$

To estimate history dependence in the observed choices, we applied both the full model and stimulus model to the choices and measured the difference of choice prediction accuracy between the two models (each 10-fold cross-validated). The rationale is that additional choice variability explained by the full model relative to the stimulus model is attributable to the choice-outcome history terms that are present only in the full model. To compare history dependence between light-on and light-off trials in our inactivation experiments, we computed history dependence separately for light-on trials and light-off trials. That is, the full model and stimulus model were fit separately for the two trial types. To match the number of trials between light-on and light-off conditions, we randomly subsampled 30 trials, 100 times in each condition, and computed the mean history dependence across 100 subsamples. In addition, we also examined whether history dependence was altered by inactivation using the history model (Equation 4). This is the method we used in our

previous publication (Hwang et al., 2017). History model weights and constants were estimated from a training set using only a subset of light-off trials, and the model accuracy was measured on light-on and light-off test trials in a separate set in a 10-fold cross-validation manner. Our rationale was that if history dependence is altered by inactivation, model accuracy for light-on trials would be worse than that of light-off trials.

Two-photon calcium imaging experiment—Mice (*Camk2a-tTA::tetO-GCaMP6s*, N = 10; or *Camk2a-tTA::tetO-GCaMP6s::Rosa-CAG-LSL-tdTomato*, N = 3) were placed in a stereotaxic frame and implanted with a head-fixation bar. In 5 mice, 100–150 nL of CAV-Cre was injected in the right STR through a bur hole as described above. In 8 mice, 40–150 nL of CAV-Cre was injected in the right pM2. Following a minimum 3 days of recovery, daily water consumption was limited to a controlled volume (typically 1 mL/day). After 3–10 days of water restriction, mice began behavioral training.

After the mouse's fraction of correct choice reached 60% in the two-choice task, we paused training and allowed unlimited water access at least for 2 days prior to craniotomy and virus injection. The craniotomy was centered in PPC of the right hemisphere. In *Camk2a-tTA::tetO-GCaMP6s* mice, 50 nL of virus encoding Cre-dependent tdTomato (AAV1-CAG-FLEX-tdTomato; UPenn Vector Core) was injected at a depth of 350 μm beneath the dura in PPC. After the injection, the craniotomy (~2 mm × 3.5 mm) was covered with an optical window fixed in place with dental cement. For *Camk2a-tTA::tetO-GCaMP6s::Rosa-CAG-LSL-tdTomato* mice, we performed a craniotomy without additional viral injections and covered it with an optical window. Following a minimum 7 days of recovery, daily water consumption was limited to a controlled volume (typically 1 mL/day). After 5–7 days of water restriction, mice resumed behavioral training.

After mice recovered the pre-surgery performance, we started imaging cortical activity at the depth of 130–430 μm with excitation at 925 nm from a Ti-Sa laser (Spectra-physics) using a two-photon microscope (B-scope, Thorlabs). For each mouse, we selected imaging fields showing a relatively high density of retrogradely labeled neurons (1–7 fields per mouse; 4 ± 2.3 fields across 13 mice). Each imaging field was 512 × 512 pixels covering 472 × 508 μm and imaging was performed at ~28.4 Hz. Each behavior-imaging session ended when the mouse was disengaged from the task, or completed 170 rewarded trials. We included for analysis all distinct PPC fields in each mouse that had at least 15 projection cells and with at least 80 successful trials. Mice completed 144 ± 26.6 (range: 80–171) rewarded trials in each imaging session.

Neural activity analysis

Single cell activity: Using custom Matlab program, fluorescence images were aligned frame by frame to compensate for lateral motions post hoc (Mitani and Komiyama, 2018). Regions of interest (ROIs) were manually drawn on the motion-corrected images by circumscribing the somas based on their GCaMP fluorescence intensity distinguishable from the background. Pixels inside each ROI were considered as a single neuron, whereas pixels extending radially outward from the soma boundary by 2–6 pixels were considered background. For each ROI, we subtracted 70% of the average background pixel intensity

from the average soma pixel intensity in each frame to adjust background contamination. The adjusted fluorescence signals were transformed to dF/F using baseline F estimated as the 8th percentile of the fluorescence signal distribution in a 20-second window. dF/F of single neurons was further transformed into an estimate of spike rates using the spike-triggered mixture model (https://github.com/lucastheis/c2s) (Theis et al., 2016).

Choice selectivity during the ITI: For each neuron, we computed the time-averaged activity in the 4-sec ITI in each trial, and performed receiver operating characteristic (ROC) analysis on the ITI activity, using the binary choice as label and the activity as score. For a given area under the ROC curve (AUROCC), double the distance from 0.5 (i.e., $2 \times |$AUROCC-0.5$|$) was taken as selectivity strength. For a significance test, we used the 95th percentile of the null distribution of the selectivity strength ($p<0.05$) estimated by choice label shuffling per neuron, 100 times.

Decoding history bias from PPC population activity: We used three different decoding methods: lasso regression, Bayesian decoder, and feedforward neural network, each described in the next sections. For all three decoders, the predictor was a population activity matrix (T trials $\times$ M neurons) and the output was a history bias vector estimated from the full model (T trials $\times$ 1). Each row of the population activity matrix corresponds to a single trial population activity vector, each element corresponding to a single neuron's time-averaged activity during the 4-second ITI. We used the same measure of performance in all decoders; the correlation coefficient between the actual and decoded biases of test trials (10-fold cross-validation). To compare decoding performance among PPC-STR, PPC-pM2, and unlabeled neuron groups while matching the population size (M), we performed a neuron dropping curve analysis (Figure 4J and Figure S3). In each session with at least 20 neurons, the subsample size decreased from 20 to 1. At each subsample size, we randomly subsampled neurons in a given session and performed decoding analyses 100 times, and computed the mean decoding performance across 100 samples. We always imaged more than 20 unlabeled neurons, so all 51 sessions were analyzed for the unlabeled group. However, we imaged at least 20 projection neurons only in 25/26 sessions that imaged PPC-STR neurons, and 10/25 sessions that imaged PPC-pM2 neurons, and only these sessions were included in the projection group analysis.

Lasso regression: The following linear equation was used to decode history bias.

$$History\ bias\ (N) = \sum_{k=1}^{M} w_k \cdot ITI\ activity\ of\ neuron_k(N) + w_0 \tag{6}$$

The weights were obtained using training trials by minimizing the following cost function, which penalized both the mean squared error of the fit and the L1 norm of the weights.

$$\frac{1}{2T}\sum_{N=1}^{T}\left(History\ bias(N) - \sum_{k=1}^{M} w_k \cdot ITI\ activity\ of\ neuron_k(N) - w_0\right)^2 + \lambda \sum_{k=1}^{M} |w_k|$$

A regularization coefficient, λ, was selected from a grid search such that it minimizes the mean squared error of the cross-validated fit.

Bayesian decoder: We implemented a Naïve Bayes decoder using the maximum a posteriori estimate based on the following formula (Glaser et al., 2017).

$$p(History\ bias(N)\ |\ ITI\ population\ activity\ (N))$$
$$= \frac{p(ITI\ population\ activity\ (N)\ |\ History\ bias(N)) \cdot p(History\ bias(N))}{p(ITI\ population\ activity\ (N))}$$

To estimate probability functions on the right side of the above equation, we discretized history bias using 10 uniformly spaced bins, and ITI activity of each neuron using 30 uniformly spaced bins. We assumed that the conditional probability of each neuron is independent from the other neurons so that we could simplify the conditional probability as follows:

$$p(ITI\ population\ activity\ (N)\ |\ History\ bias(N)) = \prod_{k=1}^{M} p(ITI\ activity\ of\ neuron_k(N)\ |\ History\ bias(N))$$

We also assumed that each conditional probability is gaussian so that we could infer the probability to observe the neural activity on a test trial, using the mean and the standard deviation estimated from training trials.

Feedforward neural network decoder: We used a neural network consisting of an input layer, a hidden layer with 10 nodes, and an output layer (Hattori et al., 2019). The input layer encoded the ITI population activity, and the output layer encoded the history bias. The hidden layer nodes computed the weighted sum of inputs and transformed it through a sigmoid transfer function. The output layer computes the weighted sum of the outputs of the hidden layer. The weights in the network was optimized from training trials using Matlab function *train* with the option, Bayesian regularization.

Multiple linear regression: We used a Matlab function *regress* to perform a multiple linear regression on the average activity during the 4-sec ITI of each neuron using two sets of predictors. In one set, we used the upcoming choice and the history bias as predictors. In the other set, we used the upcoming choice and three separable bias terms in Equation 3, i.e., outcome history bias, choice history bias, and outcome-choice interaction history bias. If the weight of a given predictor is significantly different from zero (p<0.05), we declared that the ITI activity of the neuron showed a significant weight for the predictor.

Soma inactivation experiment—Mice for inactivation experiments (*WT C57BL/6* or *Rosa26-CAG-LSL-tdTomato*; N = 15) were implanted with a head-fixation bar. In 7 mice, CAV-Cre was bilaterally injected in STR (150 nL per hemisphere) through bur holes. In 8 mice, CAV-Cre was bilaterally injected in pM2 (100 nL per hemisphere) through bur holes. In all mice, craniotomies were performed over PPC bilaterally and virus encoding Cre-dependent halorhodopsin (AAV9-EF1α-DIO-eNpHR3.0-eYFP, UPenn Vector Core; 250–750 μm beneath the dura; 100 nL per hemisphere) was injected bilaterally. The craniotomies were covered with an optical window. After the surgery and recovery, we trained mice to perform the task over a period of 2–4 months.

Once the mouse's fraction of correct choice reached 60%, we conducted 1–7 light acclimation sessions to minimize non-specific light effects on behaviors. In the acclimation sessions, the distal ends of a bifurcated fiber-optic patch cord (490 μm diameter, Doric) were placed ~2 mm above the head-fixation bar, away from PPC expressing halorhodopsin, and laser light (532 nm, 15–20 mW in each fiber, SLOC) was applied during the ITI of randomly selected 15% of trials. Most mice recovered their previous task performance within 1–2 days.

Each mouse performed both inactivation and headbar control sessions that were randomly interleaved across 7 – 12 daily sessions. In headbar control sessions, the patch cord ends were directed above the head-fixation bar, whereas in inactivation sessions they were placed directly above PPC in both hemispheres (Figure 5B). Except for this difference, all procedures were identical between headbar control and inactivation sessions. In both control and inactivation sessions, the green light was delivered in approximately 15% of randomly selected trials.

PPC-STR terminal inactivation experiment—The mice (*WT C57BL/6* or *Rosa26-CAG-LSL-tdTomato*; N = 13) were implanted with a head-fixation bar and bilaterally injected with CAV-Cre in STR and Cre-dependent halorhodopsin in PPC in the same way as the PPC-STR soma inactivation experiment. After the surgery and recovery, we trained mice to perform the task over a period of 2–4 months. Once the mouse's fraction of correct choice reached 60%, we bilaterally implanted fiber optic cannulae (200 μm core, 0.37 NA, 1.25 mm stainless steel ferrule; Newdoon) approximately 300 μm above the STR regions receiving dense projections from PPC (2.2 mm lateral, 0.8 mm posterior to bregma, 2 mm beneath the dura), and secured them to the skull using dental cement. After mice recovered their previous task performance (within 1–2 days), we performed inactivation for 2–5 days. In each inactivation session, the green laser light (532 nm, 10–15 mW for inactivation in each fiber, SLOC) was delivered in approximately 15% of randomly selected trials. After a mouse completed the terminal inactivation experiment, we perfused the mouse and checked an expression of halorhodopsin in PPC post hoc. We analyzed only the mice with clear expression in both hemispheres (N = 7).

As a control for opsin-independent non-specific effects of laser illumination in STR, such as heating (Owen et al., 2019), we performed an analogous experiment to the terminal inactivation in a separate set of mice (N = 6) in which we injected Cre-dependent eGFP (AAV1-CAG-FLEX-eGFP, UPenn Vector Core) in PPC instead of the Cre-dependent halorhodopsin.

Movement analysis—We defined movement onset as the first time after the go cue at which the joystick velocity exceeded 20 mm/sec continuously for 20 ms and the joystick moved at least 1.1 mm from the origin. Target entry was the time the joystick entered one of the two targets that were placed in two orthogonal directions (forward vs. downward) from the origin, at a distance of at least 6 mm.

<u>Trial-to-trial trajectory correlation:</u> For every pair of trials that entered the same target (forward or downward), we computed the Pearson's correlation coefficient between the two

joystick traces (the concatenated x and y position time series). The correlation coefficients computed separately for forward and downward trials were averaged. The time window for the trajectory correlation analysis was chosen to approximate the period from movement onset to target entry (0.2 ± 0.12 seconds, mean $\pm$ S.E.M. across 30 mice). Inactivation effects on trial-to-trial trajectory correlations were similar across a range of time windows between movement onset and 0.2 to 0.45 seconds from movement onset, and we present the data using a 0.2-second window.

QUANTIFICATION AND STATISTICAL ANALYSIS

Statistical details including the type of test, number of samples, p values are provided in the figures, figure legends or text. In general, we performed hypothesis tests using non-parametric bootstrap (Stout et al., 1999). In the case of bootstrap two-sample (BTS) tests that compared the means of two independent groups (μ_{group1} and μ_{group2}), we computed the null distribution for a difference in two group means under the null hypothesis that the two groups have the same means. To do so, we first removed the mean difference in the two groups by adding (μ_{group1} - μ_{group2}) to all data in group2, and then bootstrapped the mean of each group 10,000 times. If the originally observed difference (μ_{group1} - μ_{group2}) was outside the 95% confidence interval of the mean (i.e., 2.5 to 97.5th percentile in the null distribution), the null hypothesis was rejected. In the case of bootstrap paired-sample (BPS) tests, we first created single-group data that consist of differences in each pair and tested whether the mean of the differences ( ) is significantly different from zero. To compute the null distribution, we first subtracted   from all differences and bootstrapped the mean 10,000 times. If the 95% confidence interval from the null distribution did not include   , the originally observed mean, we rejected the null hypothesis that the mean difference is zero.

DATA AND CODE AVAILABILITY

The datasets and code supporting the current study have not been deposited in a public repository, but are available from the corresponding authors on request.

Supplementary Material

Refer to Web version on PubMed Central for supplementary material.

Acknowledgements

References

Abrahamyan A, Silva LL, Dakin SC, Carandini M, Gardner JL (2016) Adaptable history biases in human perceptual decisions. Proc Natl Acad Sci U S A 113:E3548–3557. [PubMed: 27330086]

Akrami A, Kopec CD, Diamond ME, Brody CD (2018) Posterior parietal cortex represents sensory history and mediates its effects on behaviour. Nature 554:368. [PubMed: 29414944]

Andersen RA, Andersen KN, Hwang EJ, Hauschild M (2014) Optic Ataxia: From Balint's Syndrome to the Parietal Reach Region. Neuron 81:967–983. [PubMed: 24607223]

Baizer JS, Desimone R, Ungerleider LG (1993) Comparison of subcortical connections of inferior temporal and posterior parietal cortex in monkeys. Vis Neurosci 10:59–72. [PubMed: 8424928]

Barthas F, Kwan AC (2017) Secondary Motor Cortex: Where 'Sensory' Meets 'Motor' in the Rodent Frontal Cortex. Trends Neurosci 40:181–193. [PubMed: 28012708]

Braun A, Urai AE, Donner TH (2018) Adaptive History Biases Result from Confidence-Weighted Accumulation of past Choices. J Neurosci 38:2418–2429. [PubMed: 29371318]

Buschman TJ, Miller EK (2007) Top-Down Versus Bottom-Up Control of Attention in the Prefrontal and Posterior Parietal Cortices. Science 315:1860–1862. [PubMed: 17395832]

Busse L, Ayaz A, Dhruv NT, Katzner S, Saleem AB, Schölvinck ML, Zaharia AD, Carandini M (2011) The Detection of Visual Contrast in the Behaving Mouse. J Neurosci 31:11351–11361. [PubMed: 21813694]

Cavada C, Goldman-Rakic PS (1989) Posterior parietal cortex in rhesus monkey: I. Parcellation of areas based on distinctive limbic and sensory corticocortical connections. J Comp Neurol 287:393–421. [PubMed: 2477405]

Chen JL, Carta S, Soldado-Magraner J, Schneider BL, Helmchen F (2013) Behaviour-dependent recruitment of long-range projection neurons in somatosensory cortex. Nature 499:336–340. [PubMed: 23792559]

Churchland MM, Santhanam G, Shenoy KV (2006) Preparatory Activity in Premotor and Motor Cortex Reflects the Speed of the Upcoming Reach. J Neurophysiol 96:3130–3146. [PubMed: 16855111]

Crammond DJ, Kalaska JF (1994) Modulation of preparatory neuronal activity in dorsal premotor cortex due to stimulus-response compatibility. J Neurophysiol 71:1281–1284. [PubMed: 8201421]

Desmurget M, Epstein CM, Turner RS, Prablanc C, Alexander GE, Grafton ST (1999) Role of the posterior parietal cortex in updating reaching movements to a visual target. Nat Neurosci 2:563. [PubMed: 10448222]

Economo MN, Viswanathan S, Tasic B, Bas E, Winnubst J, Menon V, Graybuck LT, Nguyen TN, Smith KA, Yao Z, Wang L, Gerfen CR, Chandrashekar J, Zeng H, Looger LL, Svoboda K (2018) Distinct descending motor cortex pathways and their roles in movement. Nature 563:79. [PubMed: 30382200]

Freedman DJ, Assad JA (2011) A proposed common neural mechanism for categorization and perceptual decisions. Nat Neurosci 14:143–146. [PubMed: 21270782]

Fründ I, Wichmann FA, Macke JH (2014) Quantifying the effect of intertrial dependence on perceptual decisions. J Vis 14:9–9.

Glaser JI, Chowdhury RH, Perich MG, Miller LE, Kording KP (2017) Machine learning for neural decoding. ArXiv170800909 Cs Q-Bio Stat Available at: http://arxiv.org/abs/1708.00909 [Accessed July 30, 2019].

Glickfeld LL, Andermann ML, Bonin V, Reid RC (2013) Cortico-cortical projections in mouse visual cortex are functionally target specific. Nat Neurosci 16:219–226. [PubMed: 23292681]

Guo ZV, Li N, Huber D, Ophir E, Gutnisky D, Ting JT, Feng G, Svoboda K (2014) Flow of Cortical Activity Underlying a Tactile Decision in Mice. Neuron 81:179–194. [PubMed: 24361077]

Hanks TD, Kopec CD, Brunton BW, Duan CA, Erlich JC, Brody CD (2015) Distinct relationships of parietal and prefrontal cortices to evidence accumulation. Nature 520:220–223. [PubMed: 25600270]

Harvey CD, Coen P, Tank DW (2012) Choice-specific sequences in parietal cortex during a virtual-navigation decision task. Nature 484:62–68. [PubMed: 22419153]

Hattori R, Danskin B, Babic Z, Mlynaryk N, Komiyama T (2019) Area-Specificity and Plasticity of History-Dependent Value Coding During Learning. Cell Available at: http://www.sciencedirect.com/science/article/pii/S0092867419304465 [Accessed June 10, 2019].

Hovde K, Gianatti M, Witter MP, Whitlock JR (2018) Architecture and organization of mouse posterior parietal cortex relative to extrastriate areas. bioRxiv:361832.

Hwang EJ, Dahlen JE, Mukundan M, Komiyama T (2017) History-based action selection bias in posterior parietal cortex. Nat Commun 8:1242. [PubMed: 29089500]

Hwang EJ, Hauschild M, Wilke M, Andersen RA (2012) Inactivation of the parietal reach region causes optic ataxia, impairing reaches but not saccades. Neuron 76:1021–1029. [PubMed: 23217749]

Hwang EJ, Hauschild M, Wilke M, Andersen RA (2014) Spatial and Temporal Eye–Hand Coordination Relies on the Parietal Reach Region. J Neurosci 34:12884–12892. [PubMed: 25232123]

Kim S-Y, Adhikari A, Lee SY, Marshel JH, Kim CK, Mallory CS, Lo M, Pak S, Mattis J, Lim BK, Malenka RC, Warden MR, Neve R, Tye KM, Deisseroth K (2013) Diverging neural pathways assemble a behavioural state from separable features in anxiety. Nature 496:219–223. [PubMed: 23515158]

Knowland D, Lilascharoen V, Pacia CP, Shin S, Wang EH-J, Lim BK (2017) Distinct Ventral Pallidal Neural Populations Mediate Separate Symptoms of Depression. Cell 170:284–297.e18. [PubMed: 28689640]

Lauwereyns J, Watanabe K, Coe B, Hikosaka O (2002) A neural correlate of response bias in monkey caudate nucleus. Nature 418:413–417. [PubMed: 12140557]

Lee D, Seo H, Jung MW (2012) Neural Basis of Reinforcement Learning and Decision Making. Annu Rev Neurosci 35:287–308. [PubMed: 22462543]

Lewis JW, Essen DCV (2000) Corticocortical connections of visual, sensorimotor, and multimodal processing areas in the parietal lobe of the macaque monkey. J Comp Neurol 428:112–137. [PubMed: 11058227]

Li N, Chen T-W, Guo ZV, Gerfen CR, Svoboda K (2015) A motor cortex circuit for motor planning and movement. Nature advance online publication Available at: http://www.nature.com/nature/journal/vaop/ncurrent/full/nature14178.html [Accessed February 26, 2015].

Lim BK, Huang KW, Grueter BA, Rothwell PE, Malenka RC (2012) Anhedonia requires MC4R-mediated synaptic adaptations in nucleus accumbens. Nature 487:183–189. [PubMed: 22785313]

Mahn M, Prigge M, Ron S, Levy R, Yizhar O (2016) Biophysical constraints of optogenetic inhibition at presynaptic terminals. Nat Neurosci 19:554–556. [PubMed: 26950004]

Messier JE, Chen H, Cai Z-L, Xue M (2018) Targeting light-gated chloride channels to neuronal somatodendritic domain reduces their excitatory effect in the axon. eLife 7.

Mitani A, Komiyama T (2018) Real-Time Processing of Two-Photon Calcium Imaging Data Including Lateral Motion Artifact Correction. Front Neuroinformatics 12 Available at: https://www.frontiersin.org/articles/10.3389/fninf.2018.00098/full [Accessed March 24, 2019].

Movshon JA, Newsome WT (1996) Visual Response Properties of Striate Cortical Neurons Projecting to Area MT in Macaque Monkeys. J Neurosci 16:7733–7741. [PubMed: 8922429]

Murugan M, Jang HJ, Park M, Miller EM, Cox J, Taliaferro JP, Parker NF, Bhave V, Hur H, Liang Y, Nectow AR, Pillow JW, Witten IB (2017) Combined Social and Spatial Coding in a Descending Projection from the Prefrontal Cortex. Cell 171:1663–1677.e16. [PubMed: 29224779]

Osakada F, Callaway EM (2013) Design and generation of recombinant rabies virus vectors. Nat Protoc 8:1583–1601. [PubMed: 23887178]

Owen SF, Liu MH, Kreitzer AC (2019) Thermal constraints on in vivo optogenetic manipulations. Nat Neurosci 22:1061. [PubMed: 31209378]

Pandya DN, Seltzer B (1982) Intrinsic connections and architectonics of posterior parietal cortex in the rhesus monkey. J Comp Neurol 204:196–210. [PubMed: 6276450]

Pasupathy A, Miller EK (2005) Different time courses of learning-related activity in the prefrontal cortex and striatum. Nature 433:873–876. [PubMed: 15729344]

Paxinos G, Franklin KBJ (2004) The Mouse Brain in Stereotaxic Coordinates. Gulf Professional Publishing.

Pisella L, Gréa H, Tilikete C, Vighetto A, Desmurget M, Rode G, Boisson D, Rossetti Y (2000) An 'automatic pilot' for the hand in human posterior parietal cortex: toward reinterpreting optic ataxia. Nat Neurosci 3:729–736. [PubMed: 10862707]

Platt ML, Glimcher PW (1999) Neural correlates of decision variables in parietal cortex. Nature 400:233–238. [PubMed: 10421364]

Raposo D, Kaufman MT, Churchland AK (2014) A category-free neural population supports evolving demands during decision-making. Nat Neurosci 17:1784–1792. [PubMed: 25383902]

Author Manuscript Author Manuscript Author Manuscript Author Manuscript

Ren J, Friedmann D, Xiong J, Liu CD, Ferguson BR, Weerakkody T, DeLoach KE, Ran C, Pun A, Sun Y, Weissbourd B, Neve RL, Huguenard J, Horowitz MA, Luo L (2018) Anatomically Defined and Functionally Distinct Dorsal Raphe Serotonin Sub-systems. Cell 175:472–487.e20. [PubMed: 30146164]

Samejima K, Ueda Y, Doya K, Kimura M (2005) Representation of Action-Specific Reward Values in the Striatum. Science 310:1337–1340. [PubMed: 16311337]

Schneider CA, Rasband WS, Eliceiri KW (2012) NIH Image to ImageJ: 25 years of Image Analysis. Nat Methods 9:671–675. [PubMed: 22930834]

Schwarz LA, Miyamichi K, Gao XJ, Beier KT, Weissbourd B, DeLoach KE, Ren J, Ibanes S, Malenka RC, Kremer EJ, Luo L (2015) Viral-genetic tracing of the input–output organization of a central noradrenaline circuit. Nature 524:88–92. [PubMed: 26131933]

Shadlen MN, Newsome WT (2001) Neural Basis of a Perceptual Decision in the Parietal Cortex (Area LIP) of the Rhesus Monkey. J Neurophysiol 86:1916–1936. [PubMed: 11600651]

Snyder LH, Batista AP, Andersen RA (1997) Coding of intention in the posterior parietal cortex. Nature 386:167–170. [PubMed: 9062187]

Stout WF, Marden J, Travers K (1999) Statistics: Making sense of data. Mobius Communications Ltd.

Sul JH, Jo S, Lee D, Jung MW (2011) Role of rodent secondary motor cortex in value-based action selection. Nat Neurosci 14:1202–1208. [PubMed: 21841777]

Sutton RS, Barto AG (1998) Reinforcement Learning: An Introduction. A Bradford Book.

Tai L-H, Lee AM, Benavidez N, Bonci A, Wilbrecht L (2012) Transient stimulation of distinct subpopulations of striatal neurons mimics changes in action value. Nat Neurosci 15:1281–1289. [PubMed: 22902719]

Theis L, Berens P, Froudarakis E, Reimer J, Román Rosón M, Baden T, Euler T, Tolias AS, Bethge M (2016) Benchmarking Spike Rate Inference in Population Calcium Imaging. Neuron 90:471–482. [PubMed: 27151639]

Todd JJ, Marois R (2004) Capacity limit of visual short-term memory in human posterior parietal cortex. Nature 428:751–754. [PubMed: 15085133]

Tye KM, Prakash R, Kim S-Y, Fenno LE, Grosenick L, Zarabi H, Thompson KR, Gradinaru V, Ramakrishnan C, Deisseroth K (2011) Amygdala circuitry mediating reversible and bidirectional control of anxiety. Nature 471:358–362. [PubMed: 21389985]

Wickersham IR, Lyon DC, Barnard RJO, Mori T, Finke S, Conzelmann K-K, Young JAT, Callaway EM (2007) Monosynaptic Restriction of Transsynaptic Tracing from Single, Genetically Targeted Neurons. Neuron 53:639–647. [PubMed: 17329205]

Xiong Q, Znamenskiy P, Zador AM (2015) Selective corticostriatal plasticity during acquisition of an auditory discrimination task. Nature 521:348–351. [PubMed: 25731173]

Znamenskiy P, Zador AM (2013) Corticostriatal neurons in auditory cortex drive decisions during auditory discrimination. Nature 497:482–485. [PubMed: 23636333]

Highlights

- PPC neurons projecting to STR (PPC-STR) and pM2 (PPC-pM2) form parallel subsystems.

- PPC-STR neurons represent action-selection bias more strongly than PPC-pM2 neurons.

- PPC-STR neurons receive strong inputs from association areas and bias action selection.

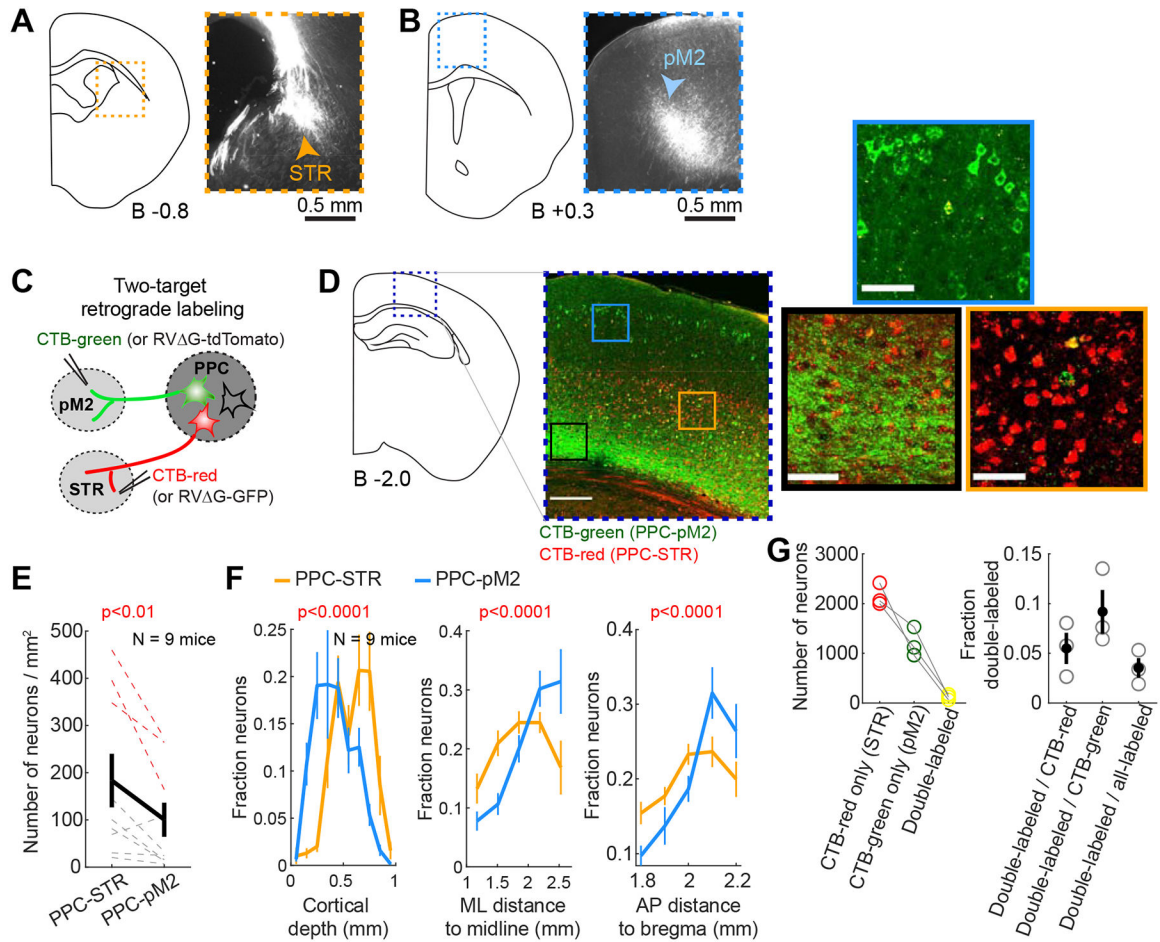- PPC-pM2 neurons receive strong inputs from sensorimotor areas and control movements.

Figure 1. PPC neurons projecting to STR (PPC-STR) and pM2 (PPC-pM2) represent largely distinct subpopulations.

A-B. Anterograde labeling of PPC projections. Left: Drawing of the right hemisphere. Right: Fluorescence image of axons of PPC projection neurons in the boxed area. The anterior-posterior distance from bregma to each coronal section is indicated at the bottom. STR: dorsal striatum. pM2: posterior secondary motor cortex.

C. Two-target retrograde labeling. In one set of mice (N = 3), CTB-red was injected in STR, and CTB-green was injected in pM2. In the other set (N = 6), RV G-GFP was injected in STR, and RV G-tdTomato was injected in pM2.

D. A coronal brain section showing PPC neurons labeled by retrograde CTB injected in STR (red) and pM2 (green). Magnified images are from three regions (blue, black, and orange boxes) in PPC. Double-positive cells are rare. The green signal in the black box is mostly from axons.

E. Density of neurons labeled by retrograde tracers injected in STR vs. pM2. Red dotted lines: 3 mice injected with CTBs. Grey dotted lines: 6 mice injected with RV G. Thick line: mean ± S.E.M. across 9 mice. BPS test.

F. Relative density histograms of retrogradely labeled neurons (mean ± S.E.M. across 9 mice) in PPC along the cortical depth, mediolateral distance to the midline, and anteroposterior distance to bregma. Orange: retrograde tracers injected in STR. Blue:

retrograde tracers injected in pM2. BPS test on the spatial centers (i.e., average positions) between the two projection groups. PPC-STR and PPC-pM2 neurons are differentially distributed within PPC.

G. PPC neurons projecting to both STR and pM2 are uncommon. Left: Total number of neurons labeled by only CTB-red injected in STR, only CTB-green injected in pM2, and both CTBs. The number of neurons labeled by both CTBs is 122 ± 32 (mean $\pm$ S.E.M. across 3 mice). Right: Fraction of neurons labeled by both CTBs (i.e., projecting to both STR and pM2) relative to CTB-red, CTB-green, and all labeled neurons. Circles: individual mice. Black lines: mean $\pm$ S.E.M. across 3 mice.
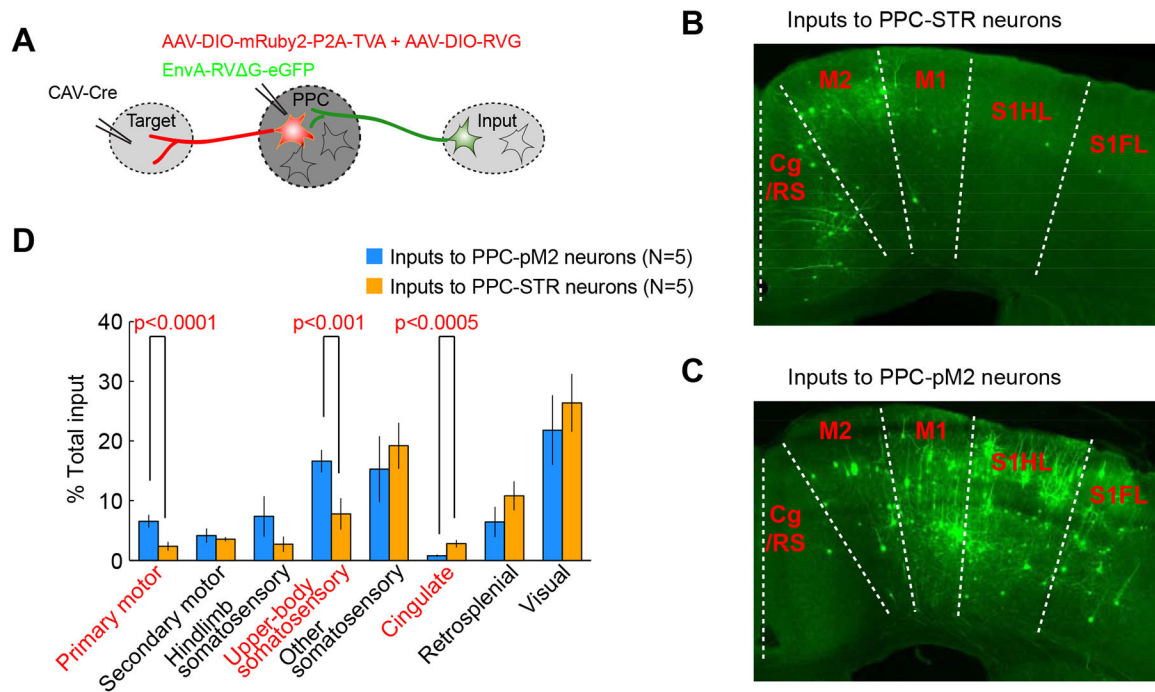
Figure 2. PPC-STR and PPC-pM2 neurons receive distinct distributions of long-range cortical inputs.

A. Schematic of projection-specific, retrograde monosynaptic tracing.

B. A coronal section showing long-range cortical inputs to PPC-STR neurons. The anterior-posterior distance from bregma is indicated on the lower left corner. Cg/RS: cingulate/retrosplenial complex (transitional zone posterior to cingulate and anterior to retrosplenial cortex). M2: secondary motor cortex. M1: primary motor cortex. S1HL: primary somatosensory cortex hindlimb region. S1FL: primary somatosensory cortex forelimb region.

C. A coronal section showing long-range cortical inputs to PPC-pM2 neurons.

D. Quantification of dorsal cortical inputs to PPC-STR vs. PPC-pM2 neurons (N = 5 mice each). The y-axis represents the percentage of inputs, normalized to the total inputs in each mouse. Mean ± S.E.M. across 5 mice. BTS test.
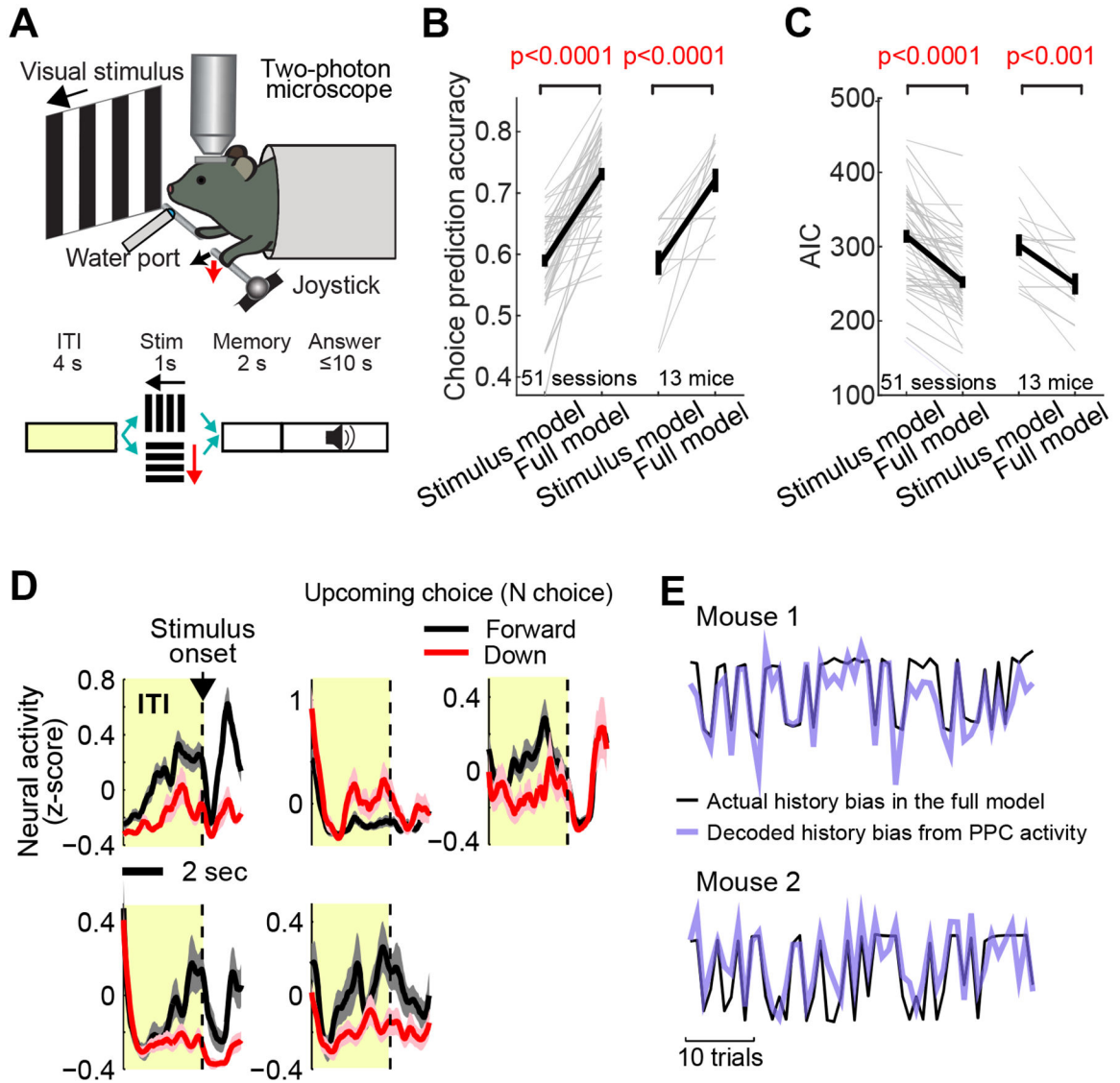
Figure 3. PPC neurons represent history bias in two-choice task.

A. Schematic of the two-choice joystick task.

B. The choice prediction accuracy of stimulus model vs. full model across 51 imaging sessions (left, green) in 13 mice (right, black). The stimulus model uses stimulus and constant as predictors, and the full model uses stimulus, constant, and history information. Thin lines: individual sessions or mice. Thick lines: mean ± S.E.M. BPS test. History has a significant impact on choice.

C. The Akaike information criteria (AIC) of stimulus model vs. full model across 51 sessions (left) in 13 mice (right). BPS test. The smaller the AIC, the better the prediction.

D. The mean activity of example neurons in PPC during the inter-trial interval (ITI) and stimulus period of the two-choice task. Black: mean ± S.E.M. across all forward choice trials in one imaging session (202 for the top three neurons and 65 for the bottom two neurons). Red: mean ± S.E.M. across all downward trials in the same session (65 and 137

for the top and bottom row neurons, respectively). These neurons show tuning to the upcoming (N) choice during the ITI (i.e., N-choice tuning).

E. Example traces of trial-by-trial history bias estimated from the full model (black; Equation 3) and a lasso regression fit (purple, cross-validated) by the ITI activity of a population of PPC neurons, indicating that the PPC population represents the history bias. In the lasso regression, history bias in each trial was decoded from a weighted sum of the ITI activity of all imaged PPC neurons (STAR Methods).
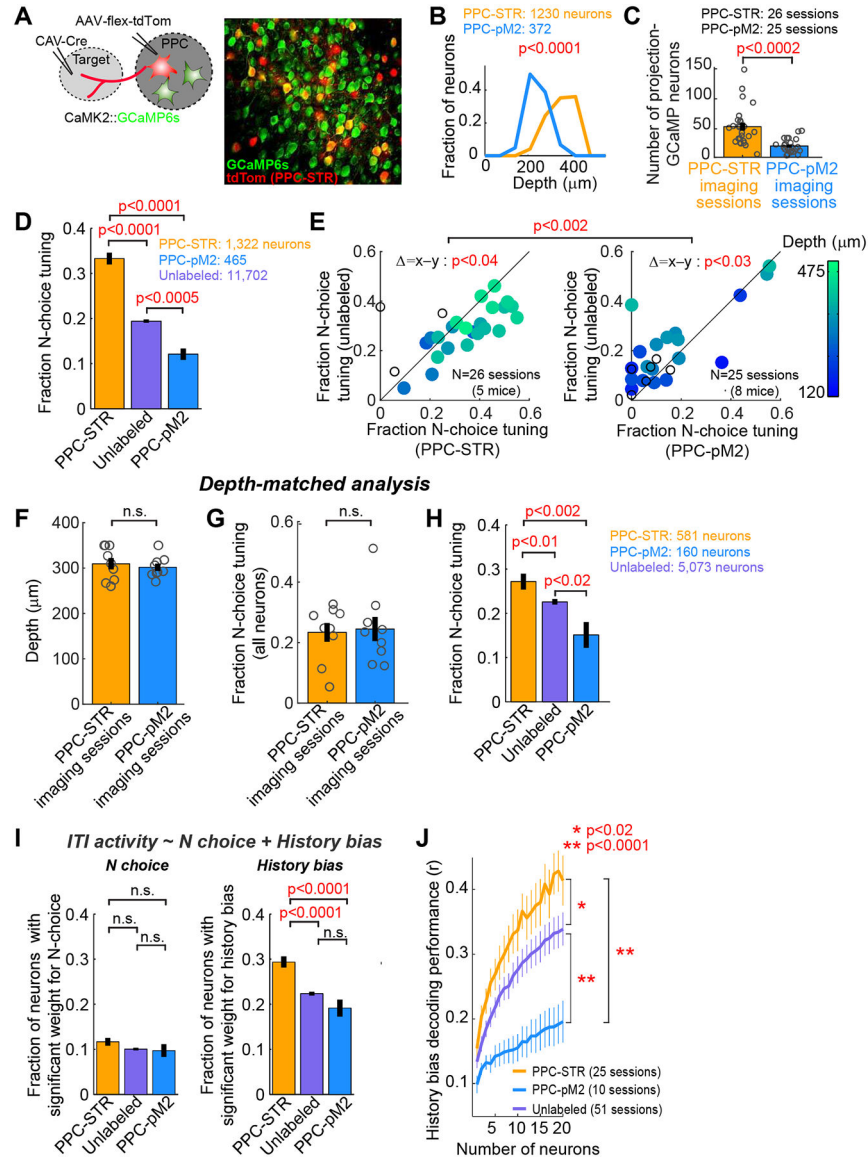
Figure 4. History bias is preferentially encoded by PPC-STR neurons.

A. PPC-STR or PPC-pM2 neurons were retrogradely labeled with tdTomato in mice expressing GCaMP6s in excitatory neurons. Right: an example PPC imaging field.

B. Histograms of the fractions of imaged projection neurons along cortical depth. Orange: PPC-STR neurons. Blue: PPC-pM2 neurons. BTS test. PPC-STR neurons tend to reside in deeper layers than PPC-pM2 neurons.

C. The number of neurons that were retrogradely labeled and showed detectable GCaMP signals in the field of each imaging session (1 field / session). Circles: individual sessions (26 PPC-STR and 25 PPC-pM2 sessions from 5 and 8 mice, respectively). Black line: mean ± S.E.M. across sessions. BTS test.

D. The fraction of neurons that are significantly tuned to the upcoming choice during the ITI (N-choice tuning) for PPC-STR, unlabeled, and PPC-pM2 neurons. Data were pooled across

animals. Error bar: S.E. χ^2 test. PPC-STR neurons are more likely tuned to N choice than PPC-pM2 and unlabeled neurons.

E. Within-session comparison of the fraction of N-choice tuning during the ITI; PPC-STR vs. unlabeled population (left) or PPC-pM2 vs. unlabeled population (right). Each dot: single session (1 field / session). The imaging depth of each session is color coded. Open dots: sessions with no depth information. BPS test on the fraction of N-choice tuning between projection and unlabeled neurons. BTS test on differences in the fraction of N-choice tuning (projection – unlabeled) between the two projection groups.

F. A subset of imaging sessions were selected in which the imaging depths were between 250 and 350 m to match the depths between the two projection groups (N = 9 sessions per group). Circles: individual sessions. Black line: mean ± S.E.M. across sessions. BTS test.

G. Depth-matched comparison of the fraction of neurons with N-choice tuning during the ITI in the general population of PPC neurons between the depth-matched PPC-STR vs. PPC-pM2 imaging sessions. All GCaMP6s-positive neurons were included in this analysis regardless of tdTomato expression. Circles: individual sessions. Black line: mean ± S.E.M. across sessions. BTS test. The responses of all imaged neurons are similar between the two depth-matched imaging groups.

H. Depth-matched comparison of the fraction of neurons with N-choice tuning during the ITI in three PPC subpopulations, PPC-STR, unlabeled, and PPC-pM2 neurons. Data from the depth-matched sessions were pooled across animals. Error bar: S.E. χ^2 test. Even when the depths were matched, PPC-STR neurons are more likely tuned to N choice than unlabeled and PPC-pM2 neurons.

I. The fraction of neurons whose ITI activity showed significant weights for N choice (left) or history bias (right) in a multiple linear regression. Data were pooled across animals. Error bar: S.E. χ^2 test. PPC neurons, especially PPC-STR neurons, encode history bias more preferentially than N choice.

J. The estimated trial-by-trial history bias (Equation 3) was decoded from the ITI activity of each neuronal population, similar to Figure 3E (STAR Methods). Decoder performance was measured as the Pearson's correlation coefficient between the decoded bias and actual bias. The number of neurons in three populations was matched by subsampling (1 to 20 neurons). For each projection population, only the sessions with at least 20 projection neurons were included. Mean ± S.E.M. across sessions. BTS test on the average across all population sizes. History bias is encoded preferentially by PPC-STR neurons.
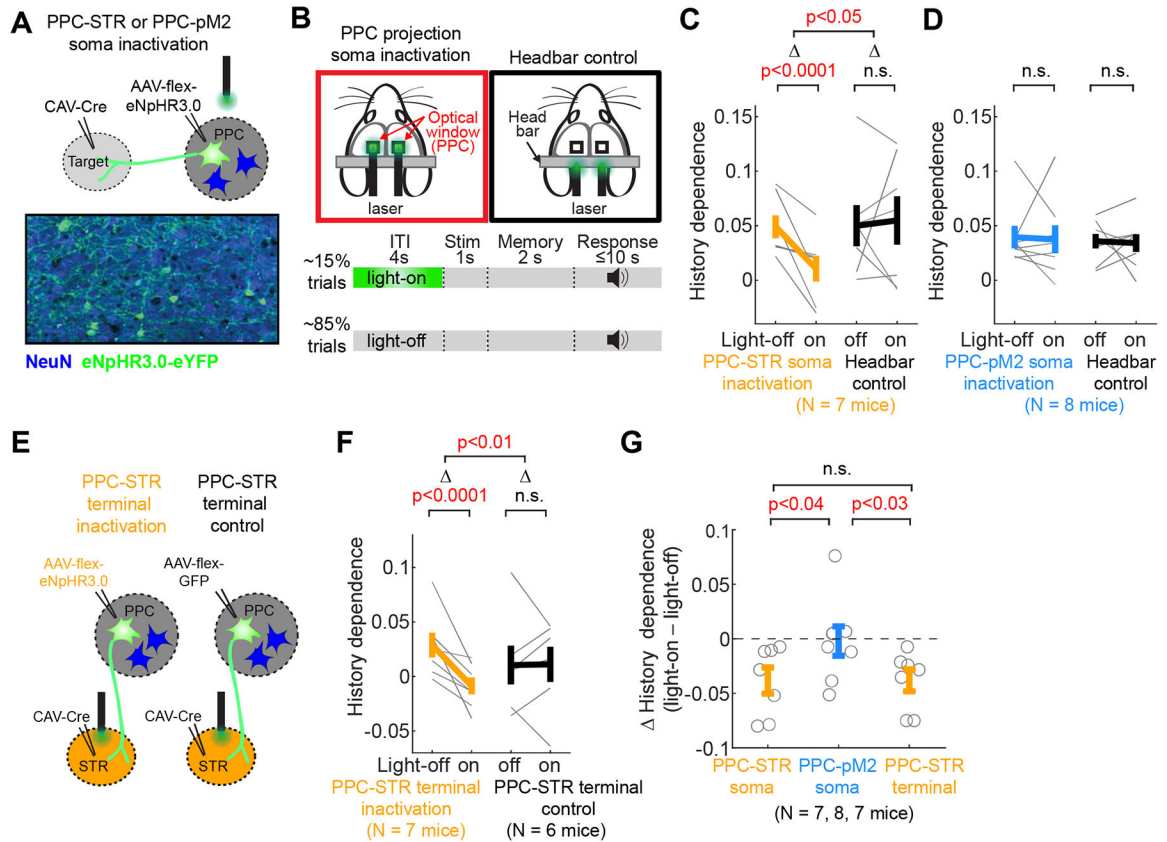
Figure 5. Inactivating the PPC-STR pathway weakens history bias.

A. Selective expression of halorhodopsin in projection neurons in PPC.

B. Each mouse performed both soma inactivation and headbar control sessions that were randomly interleaved (one session / day). In inactivation sessions, a bifurcated optical patch cord was placed over PPC bilaterally. In headbar control sessions, the patch cord was placed above the headbar. In both session types, green light (532 nm) was delivered during the ITI of 15% of randomly selected trials.

C. History dependence (full model accuracy – stimulus model accuracy) in light-off vs. light-on trials (10-fold cross-validated) in inactivation (left) and headbar control (right) sessions. Mice (N = 7) expressed halorhodopsin in PPC-STR neurons. Thin lines: individual mice. Thick lines: mean ± S.E.M. across mice. As inactivation and headbar control data were collected from the same mice, BPS tests were applied to both within-group (light-off vs. light-on) and between-group (inactivation vs. control) comparisons. Between-group comparison was made on light effects (D; light-on trials - light-off trials). Inactivation of PPC-STR neurons reduced history dependence.

D. The same as **C**, but for mice (N = 8) expressing halorhodopsin in PPC-pM2 neurons. Inactivation of PPC-pM2 neurons did not reduce history dependence.

E. PPC-STR axon terminal inactivation experiment. In the inactivation group (left), halorhopdoin was expressed in PPC-STR neurons. In the control group (right), GFP was expressed in PPC-STR neurons. Fiber optic cannulae were implanted in STR bilaterally.

F. The same as **C**, but the green light was delivered to STR at the axon terminals of PPC-STR neurons. Separate sets of mice performed inactivation (N = 7 mice) and control (N = 6

mice) sessions; thus, BPS and BTS tests were applied to within-group and between-group comparisons, respectively. Inactivation of STR axon terminals of PPC-STR neurons reduced history dependence.

G. Inactivation effect measured as change of history dependence (light-on trials – light-off trials) by the inactivation of PPC-STR somas, PPC-pM2 somas, and PPC-STR axon terminals in STR. BTS test. Soma and terminal inactivation of PPC-STR neurons selectively reduced history dependence.
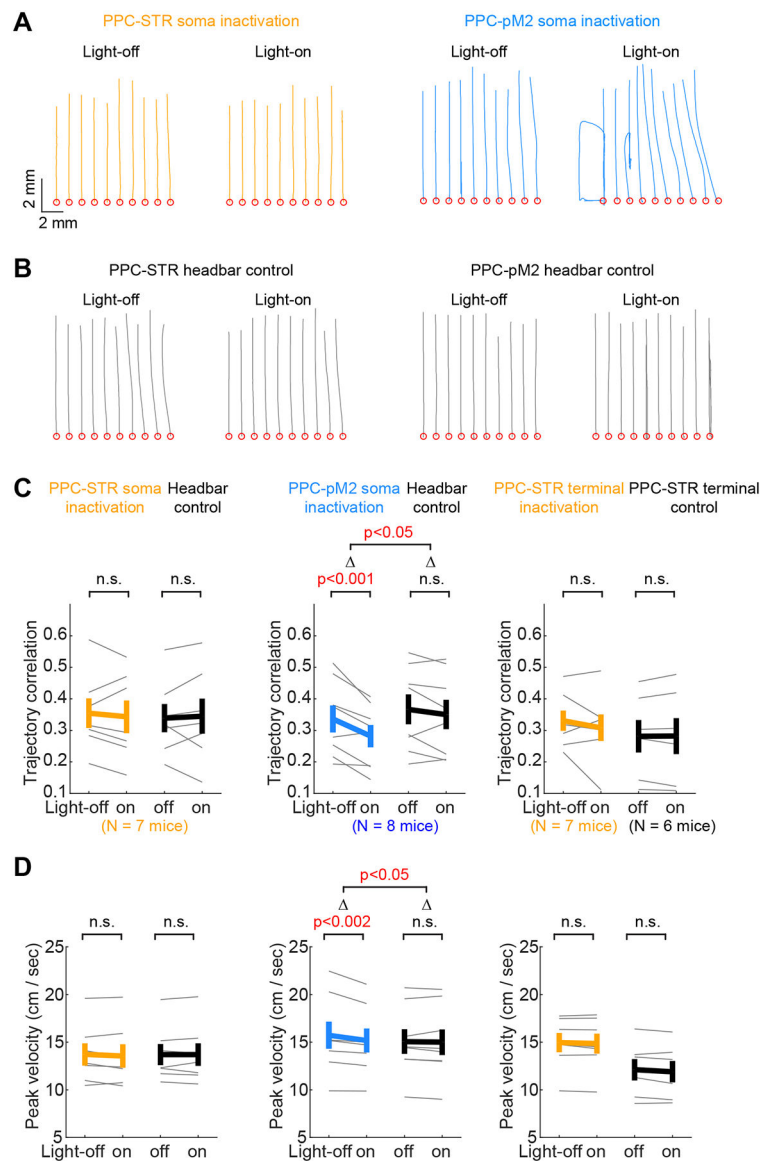
Figure 6. Inactivating PPC-pM2 neurons alters movement kinematics.

A. Trajectories of movements from movement onset to the target (forward), in example PPC-STR versus PPC-pM2 soma inactivation sessions. Thin lines: 10 trials in each light condition. Red circles: the origin of movements.

B. The same as **A**, but for example headbar control sessions.

C. Trial-to-trial correlation of movement trajectories on light-off vs. light-on trials (STAR Methods). The higher the correlation coefficient, the more consistent/similar the movements. The same sessions used for the analysis of history dependence (Figure 5) were subjected to kinematic analysis. Left: PPC-STR soma inactivation group (N = 7 mice). Middle: PPC-pM2 soma inactivation group (N = 8 mice). Right: PPC-STR axon terminal inactivation (N = 7 mice) group and control group (N = 6 mice). BPS tests were applied to all within-group comparisons (light-off vs. light-on). For between-group comparisons (inactivation vs. control), BPS test in soma inactivation groups, and BTS test in terminal groups. Thin lines:

individual mice. Thick lines: mean ± S.E.M. across mice. Inactivation of PPC-pM2 neurons reduced trial-to-trial consistency of movement trajectories.

D. The same as **C**, but for the peak velocity of movements. Inactivation of PPC-pM2 neurons reduced the peak velocity of movements.
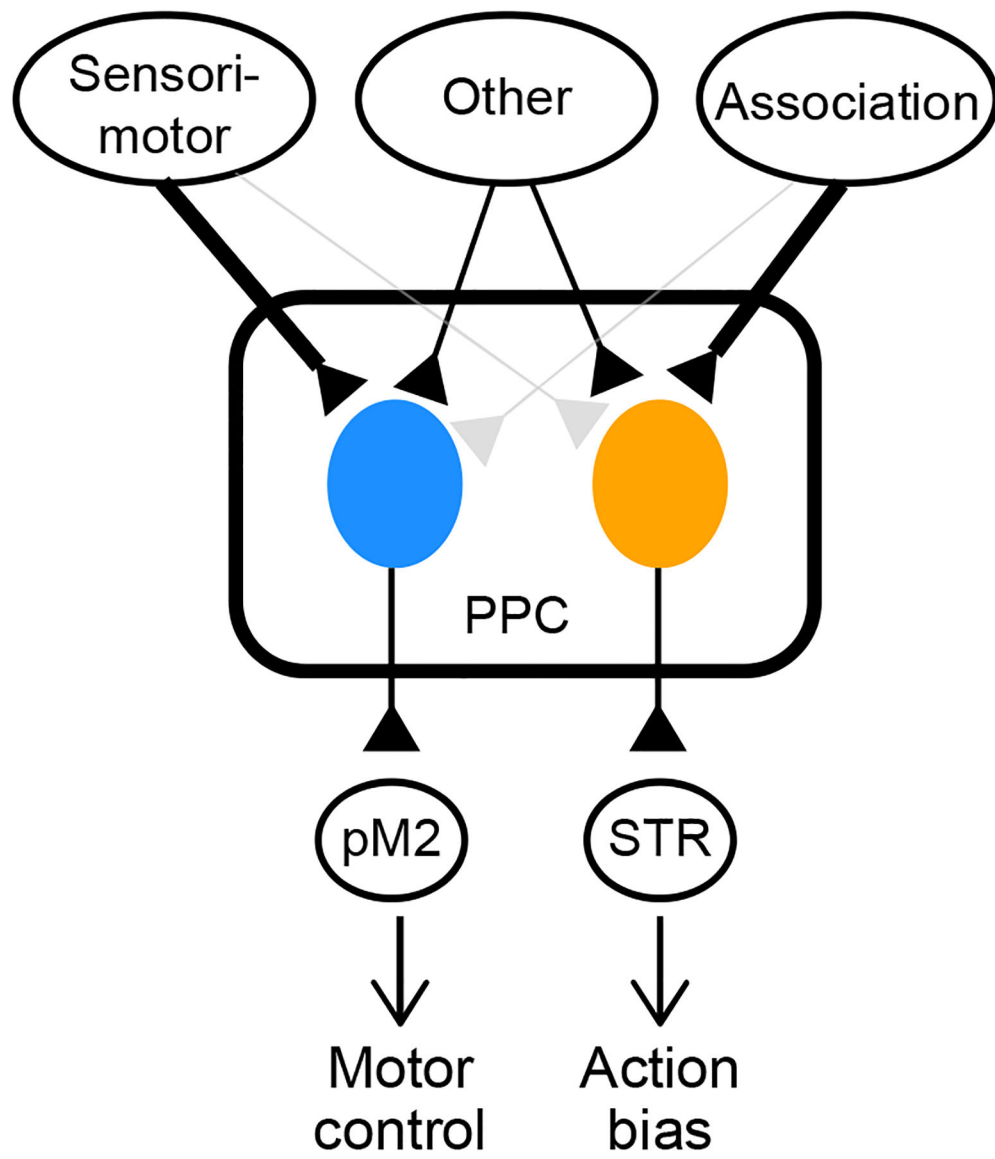
Figure 7. PPC serves multiple functions through a pathway-specific functional division.
Schematic of parallel subsystems in PPC. PPC neurons involved in biasing action selection receive stronger inputs from association areas and project to STR. PPC neurons involved in the control of movements receive stronger inputs from sensorimotor areas, and project to pM2.

KEY RESOURCES TABLE

REAGENT or RESOURCE	SOURCE	IDENTIFIER
Bacterial and Virus Strains		
AAV-DJ-EF1α-DIO-mRuby2-P2A-TVA	Lim Lab	N/A
AAV-DJ-EF1α-DIO-RVG	Lim Lab	N/A
EnvA-RV G-eGFP	Lim Lab	N/A
RV G-GFP	Lim Lab	N/A
RV G-tdTomato	Lim Lab	N/A
CAV-Cre	BioCampus	N/A
AAV1-CAG-tdTomato	UPenn Vector Core	Addgene: 105554-AAV1
AAV1-CAG-FLEX-tdTomato	UPenn Vector Core	Addgene: 51503-AAV1
AAV1-CAG-FLEX-eGFP	UPenn Vector Core	Addgene:51502-AAV1
AAV9-EF1α-DIO-eNpHR3.0-eYFP	UPenn Vector Core	Addgene: 26966-AAV9
Chemicals, Peptides, and Recombinant Proteins		
CTB-Alexa-Fluor 594 conjugate	Thermo Fisher	Cat#C22842
CTB-Alexa-Fluor 488 conjugate	Thermo Fisher	Cat#C22841
Experimental Models: Organisms/Strains		
Mouse: wild-type (C57BL/6)	Charles River Laboratories	Strain Code:027
Mouse: B6.Cg-Gt(ROSA)26Sor[tm14(CAG-tdTomato)Hze]/J; also known as Rosa26-CAG-LSL-tdTomato	The Jackson Laboratory	Cat#007914
Mouse: B6.CBA-Tg(Camk2a-tTA)1Mmay/J; also known as Camk2a-tTA	The Jackson Laboratory	Cat#003010
Mouse: B6.DBA-Tg(tetO-GCaMP6s)2Niell/J; also known as tetO-GCaMP6s	The Jackson Laboratory	Cat#024742
Software and Algorithms		
MATLAB v. 2014a & 2019a	MathWorks	RRID: SCR_001622
ImageJ FIJI	Schneider et al., 2012	RRID: SCR_002285
Bootstrap test	Stout et al., 1999	N/A
Spike-triggered mixture model	Theis et al., 2016	https://github.com/lucastheis/c2s
Lateral motion correction of calcium images	Mitani and Komiyama, 2018	N/A